Advanced Composites and Hybrid Materials (2026) 9:235
https://doi.org/10.1007/s42114-026-01862-z

RESEARCH

Oxygen-scavenging MnO_2 nanoparticles enabled thermally stable and oxidation-resistant MXene inks for 3D-printed flexible asymmetric supercapacitors

Ali Shan[1] · Habibulla Imran[1] · Nida Nawaz[3] · Chenhao Cong[4] · Seung Goo Lee[5] · Komal Gola[6] · Mirza Mahmood Baig[5] · Hyungsub Yoon[7] · Jinhua Sun[6] · Se Hyun Kim[4] · Byungil Hwang[2] · Sooman Lim[1]

Received: 19 February 2026 / Revised: 5 May 2026 / Accepted: 11 May 2026
© The Author(s) 2026

Abstract

MXenes have emerged as promising candidates for flexible and printed energy storage systems due to their metallic electrical conductivity and hydrophilicity. However, their practical application is severely hindered by the restacking of delaminated sheets and rapid oxidative degradation under ambient or elevated temperatures. To address these critical challenges, we propose a strategy using redox-active 0D manganese dioxide (MnO_2) nanoparticles decorated on 2D MXene sheets to serve as effective oxygen scavengers. Density functional theory (DFT) simulations and X-ray photoelectron spectroscopy (XPS) analyses confirm that MnO_2 preferentially interacts with oxygen species, thereby significantly mitigating the oxidation of the MXene backbone. Furthermore, by incorporating 1D silver nanowires (AgNWs) to optimize ink rheology and conductivity, we developed a 0D/1D/2D hybrid ink capable of direct ink writing (DIW) 3D printing without the need for additional metal current collectors. The resulting fully printed asymmetric supercapacitor exhibited a high areal capacitance of 565.1 mF cm^{-2} and an areal energy density of 0.2 mWh cm^{-2}. Notably, the device demonstrated exceptional durability with 98.52% capacitance retention after 10,000 charge-discharge cycles and maintained stable electrochemical performance across a wide temperature range from 10 to 50 °C. This work presents a robust solution for overcoming the intrinsic instability of MXenes, paving the way for reliable, high-performance flexible electronics.

Keywords Asymmetric supercapacitor · DIW · High cyclic stability · MXene · Temperature endurance

Ali Shan and Habibulla Imran contributed equally.

✉ Jinhua Sun
jinhua@chalmers.se

✉ Se Hyun Kim
shkim97@konkuk.ac.kr

✉ Sooman Lim
smlim@jbnu.ac.kr

Byungil Hwang
bihwang@cau.ac.kr

[1] Graduate School of Flexible and Printable Electronics, LANL– JBNU Engineering Institute, Jeonbuk National University, Jeonju 54896, Republic of Korea

[2] School of Integrative Engineering, Chung-Ang University, Seoul 06974, Republic of Korea

[3] Department of Chemistry, University of Narowal, Narowal, Punjab 51600, Pakistan

[4] Department of Materials Science & Engineering, Advanced Materials Program, Konkuk University, Seoul 05029, Republic of Korea

[5] Polymers Material Lab, Department of Chemistry, University of Ulsan, Ulsan 44610, Republic of Korea

[6] Department of Industrial and Materials Science, Chalmers University of Technology, Gothenburg SE-41258, Sweden

[7] Department of Intelligent Semiconductor Engineering, Chung-Ang University, Seoul 06974, Republic of Korea

Published online: 19 May 2026

1 Introduction

Advancements in smart, stretchable electronics and the Internet of Things (IoT) for various applications such as displays, artificial electronic skins, wearable sensors, and energy storage devices have stimulated researchers' interest in developing compatible energy storage devices that can be stretched, deformed, and integrated with a variety of stretchable devices [1, 2]. Among all energy storage devices, supercapacitors exhibit positive sides of all, such as excellent power density, energy density, and cycling stability [3, 4]. To satisfy these requirements, careful consideration of the synthesis process, active materials (high mechanical strength and electrochemical performance), and electrolytes is necessary [5]. MXenes are considered the most rapidly expanding two-dimensional (2D) material family in recent years and are commonly synthesized by etching A element atomic layers from the precursor MAX phase [6, 7]. Various techniques have been used for the selective etching of A atomic layers, such as hydrofluoric acid (HF) etching [8], aqueous ammonium hydrogen bifluoride (NH_4HF_2) [9], molten salts [10], and LiF-HCl [11] ligand pair etching. Among the methods discussed above, the LiF-HCl ligand pair is the most popular method due to in situ HF formation, which eliminates the direct handling of HF. Furthermore, the LiF-HCl etchant provides additional Li ions that spontaneously intercalate into the MXene layers, which reduce the interactions between the MXene layers, leading to the enlarged interlayer distance [12, 13]. Single-layer MXene tends to restack and aggregate, owing to strong van der Waals interactions between the layers. However, the exposed surface with the easily accessible to the charge carriers is very important for the high electrochemical performance of MXene based electrode. To address this problem, various strategies have been utilized, such as the insertion of transition metal oxides [14], activated carbon [15], and metal cations [16]. Among these, the intercalation of metal oxides allows the formation of stable delaminated MXene structures due to their physical separation role together with the good chemical and thermal stability, which is responsible for maintaining the stable integrity of MXene and providing additional active sites for electrolyte ion storage [17]. Luo et al. synthesized 1D/2D Fe_2O_3/MXene composites for all-solid-state supercapacitors, and a high areal capacitance (691mF cm^{-2}) but poor cyclic stability (81.74%) were achieved [18]. Similarly, Zhang et al. synthesized a Co_3O_4 nanoparticle-MXene composite with enhanced specific capacitance (1081 F g^{-1}), energy density (26.06 Wh kg^{-1}), and power density (700 W kg^{-1}), however, the capacity retention is only about 83% after 8000 cycles [19] due to the poor stability of the composites. Chavan et al. fabricated an asymmetric supercapacitor using NiO@MXene as anode and copper oxide as cathode, which delivered a high specific capacitance (1542 F g^{-1}) and relatively lower energy density (10.7 Wh kg^{-1}) and cyclic stability (90.6%) after 5000 cycles [20]. Moreover, our recent study demonstrated a better areal capacitance (138.75 mF cm^{-2}), however, the supercapacitor made by MXene still suffers from poor stability with only 78.7% capacitance retention [21]. The poor cyclic stability for all MXene-based composites is mainly due to the decomposition of MXene during the charging and discharging process. It has been well-known that the MXene can be easily oxidized with the formation of the TiO_2. Therefore, it is highly demanded to develop efficient strategies to stabilize the MXene and prevent its decomposition during the charging/discharging process in a water-based supercapacitor system.

MnO_2 is a typical metal oxide with high (+4) and variable oxidation states (+2 to +4), making it a promising redox-active component for electrochemical energy-storage systems [22]. Chen et al. synthesized hollow MnO_2 nanoparticles and demonstrated their reactive oxygen species (ROS)-scavenging ability as an artificial nano-enzyme in osteoarthritis [23]. Although this study was not conducted in a MXene-based system, it highlights the redox-active and oxygen-interacting nature of MnO_2. In the present study, we investigate whether such redox-active MnO_2 nanoparticles can contribute to mitigating MXene oxidation when uniformly integrated with MXene sheets. Therefore, understanding the interface and interaction between MXene and MnO_2 is important for designing stable MXene-based electrodes.

In addition, although MXene is conductive, after the incorporation with MnO_2, a current collector is still required to increase the conductivity of the electrode after coating the MXene and MnO_2 composite based on the inject printing method. Moreover, in order to further increase the electrical conductivity, activated carbon [24], carbon nanotubes [24, 25], gold [25, 26], and silver are usually added to the electrode as conductive additives. Gold exhibits exceptional conductivity but is extremely expensive, thus limiting practical applications. The active carbon and carbon nanotube particles render the formed electrode brittle, which reduces the stability of the fabricated printed electrodes, limiting their potential applications. AgNWs are viable materials that are conductive, flexible, and cost-effective. The chemical nature of silver provides high conductivity, and its one-dimensional (1D) morphology confers excellent flexibility [27, 28]. The addition of highly conductive AgNWs not only provide one dimensional conductive network in the electrode, but it could also allow the fabrication of a current collector-free electrode [29]. Therefore, the synergy of the three different materials with different dimensions from zero-dimensional (0D)-MnO_2, to 1D-AgNWs, and

to 2D-MXene layers can strategically address all the challenges in using MXene as electrode materials for a supercapacitor with high performance, flexibility, and stability.

In this study, the redox-active functionalization of 2D-MXene sheets using 0D-MnO_2 nanoparticles (NPs) was introduced with two aims, one is to prevent the agglomeration issue of MXene by the intercalation of the small MnO_2 nanoparticles; the second one is to act as oxidation scavenger to completely prevent the oxidation and decomposition of the MXene, thus increasing it chemical stability and cycling stability of the supercapacitor. The incorporation of the 1D-AgNWs will not only increase the conductivity by bridging the MXene 2D nanosheet with 1D conductive wires but also allow direct printing of the MXene/MnO_2 on the surface of the substrate without the pre-deposition of the current collector contact. This research presents a methodology for combining the materials with various morphologies and dimensions to address the challenges associated with MXene, including poor cyclic stability, fewer redox active sites, susceptibility to oxidation, and reduced conductivity following intercalation and functionalization demands of foreign current collectors.

2 Materials and methods

2.1 Materials

MXene precursor MAX powder (Ti_3AlC_2, 99%), manganese (II) nitrate tetrahydrate ($Mn(NO_3)_2{\cdot}4H_2O$, 99.9%), hydrochloric acid (HCl, 37%), lithium fluoride (LiF, 99%), carbon cloth (400 mesh), sodium hydroxide (NaOH, 98%), sulfuric acid (H_2SO_4, 98%), Nafion (5%), polyvinyl alcohol (PVA, 99%), silver nanowires (AgNWs, 98%) and polyethylene terephthalate (PET) were obtained from Sigma Aldrich. Moreover, the solvents distilled water and ethanol were purchased from Science 4U. All chemicals were used as received without further treatment.

2.2 Synthesis of MXene

MXene etching was performed using the LiF/HCl MILD method. First, concentrated HCl was diluted to a 9 M aqueous solution in 10 mL of double-distilled water. Subsequently, 0.75 g of LiF was added to the HCl solution and stirred at 50 °C for 2 h to obtain a homogeneous acidic etching solution. Thereafter, 0.325 g of Ti_3AlC_2 MAX phase was gradually added to the LiF/HCl solution to avoid rapid heat generation and splashing. The reaction was allowed to proceed for 48 h, during which in situ generated HF selectively etched the Al layers from Ti_3AlC_2 and dissolved them into the solution as Al^{3+} species, leaving behind Al-free, surface-terminated $Ti_3C_2T_x$ MXene [30]. The reaction mixture was then centrifuged at 3500 rpm using distilled water and ethanol until the solution pH exceeded 5.5 to remove residual salts and acidic species. The obtained sediment was subsequently ultrasonicated for 1 h to delaminate the MXene layers, followed by overnight drying at 60 °C to obtain the final MXene product.

2.3 Synthesis of MnO_2 via the co-precipitation method

MnO_2 nanoparticles were synthesized using a facile, eco-friendly, and cost-effective method. In this process, manganese (II) nitrate tetrahydrate (6.27 g) was dissolved in 50 mL of distilled water through vigorous stirring at 60 °C, resulting in a 0.5 M solution. This procedure was continued until homogeneous dispersions of the respective salts were achieved. Subsequently, to obtain controlled reaction kinetics, a 2 M ammonium water solution was added dropwise until the solution reached a pH of 10. The solution was then washed repeatedly with distilled water and ethanol in a centrifuge. Following subsequent washing, the precipitate was dried overnight in an oven and calcined at 450 °C for 4 h to obtain the final yield.

2.4 Synthesis of MnO_2@MXene

Decoration of MnO_2 on the delaminated MXene nanosheets was achieved using a simple ultrasonication method. To maintain the temperature of the ultrasonicator, water was continuously flowed through it. First, 100 mg of the synthesized MXene powder was ground, dispersed in 50 mL of distilled water, and sonicated until the MXene powder was fully dispersed. Subsequently, 20 mg of the finely ground MnO_2 powder was added to the MXene dispersions. Ultrasonication was conducted for 2 h to ensure uniform decoration of MnO_2 nanoparticles on the MXene nanosheets. Following this process, the solution was repeatedly washed with water and ethanol to remove unreacted species, followed by overnight drying at 60 °C in a vacuum oven to obtain the final product.

2.5 Synthesis of MXene/AgNWs

MXene/AgNWs composites were synthesized using a facile ultrasonication method. The synthesis of MXene in aqueous media results in the surface termination of –OH and –F groups. These functional groups facilitate the formation of hydrogen bonds and van der Waals interactions with the metal oxides and MXene. First, 100 mg of MXene was dispersed in 50 mL of distilled water and sonicated for 1 h to ensure uniform dispersion and delamination of the MXene

sheets. Thereafter, 20 mg of 1D-AgNWs were added to the mixture and sonicated for an additional hour. The temperature within the sonicator was maintained through continuous water flow, which was crucial for the stability of the MXene. The fabricated composite was washed with distilled water and ethanol to remove unreacted MXene and AgNWs, yielding a pure composite. Finally, the composite was dried in a vacuum gas oven at 60 °C.

2.6 Synthesis of MnO_2@MXene/AgNWs composite

The synthesized MnO_2@Mxene powder was ground thoroughly, and approximately 90 mg was dispersed in 50 mL of distilled water using ultrasonication. The temperature inside the sonicator was maintained using continuous water flow. Subsequently, a homogenous dispersion of approximately 20 mg of AgNWs was added, and the mixture was sonicated for 2 h. Subsequently, the mixture was washed with distilled deionized water and ethanol to remove undesired products. The final slurry was dried overnight under vacuum to obtain the final composite for use in electrochemical supercapacitors. The overall fabrication process of MnO_2@MXene/AgNWs is illustrated in Figure S1.

2.7 Carbon cloth treatment

Carbon cloth was used as the substrate to fabricate a highly flexible, chemically stable, and mechanically stable electrode. Commercially available carbon cloth cannot be directly employed as a substrate due to its hydrophobic nature and contamination. The activation and purification steps involved treatment of carbon cloth in a 2 M HCl solution for 8 h. Subsequently, the treated cloth was washed with distilled water and further treated for 8 h in a 2 M NaOH solution. The substrate was then washed with ethanol and distilled water and dried at 60 °C to obtain the finally activated substrate with a highly hydrophilic nature, which facilitates enhanced interaction between the electrolyte and electrode. The activated hydrophilic carbon cloth substrate was then cut into 1.0 cm lengths and widths for the final fabrication of the active material.

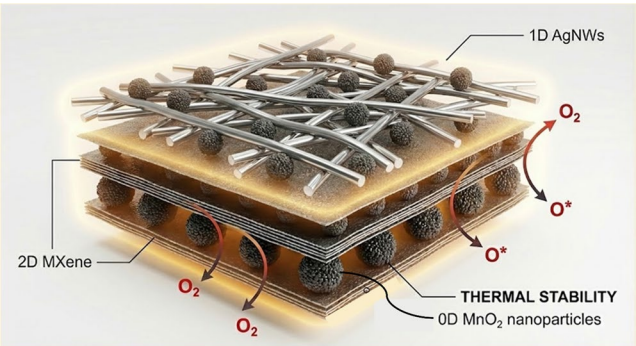


Fig. 1 Shows the schematic illustration of the thermally stable 0D/2D/1D MnO_2@MXene/AgNWs heterostructure. The 0D MnO_2 nanoparticles are anchored on the surfaces and edges of 2D MXene sheets to prevent severe agglomeration and to act as oxidation scavengers, converting atmospheric oxygen (O_2) into adsorbed oxygen species (O*) to mitigate oxidation. The 1D AgNWs network on the surface provides high electrical conductivity, contributing to the device's stability under elevated-temperature conditions

2.8 Electrode fabrications on carbon cloth for the three-electrode system

The synthesized MXene powder was pulverized before electrode fabrication. Approximately 10 mg of pulverized MXene powder was carefully added to 1 ml of 2% Nafion in ethanol as a binder. Subsequently, the mixtures were subjected to ultrasonication under a continuous flow of water to maintain the temperature required for MXene stability. After continuous ultrasonication of the mixture for 1 h, it was drop-cast onto a pre-treated carbon cloth substrate. Electrode fabrication was completed in five cycles, during which the loaded material was dried in an oven for 1 h until the entire material was deposited onto the substrate.

2.9 Preparation of MnO_2@MXene/AgNWs printable ink for two-electrode system and DIW

MnO_2@MXene/AgNWs ink for DIW was synthesized using the following methodology: First, 180 mg MnO_2@MXene/AgNWs powder and ~20 mg polyvinylidene fluoride were thoroughly ground using a mortar and pestle at a weight ratio of 90:10. 5 mL of *N*-methyl-2-pyrrolidinone solvent was added to the above mixture to obtain a homogeneous slurry, corresponding to a total solid content of 200 mg (40 mg mL^{-1}), and stirred vigorously for 48 h. Subsequently, the resulting slurry was processed with a planetary centrifugal agitator for 20 min to eliminate air bubbles introduced during the agitation process. To print the fabricated material, the as-synthesized ink was transferred to a syringe with a 22-gauge nozzle and loaded onto a DIW printer. The fabricated material ink was printed (area: 2 cm × 2 cm) on flexible PET substrate and dried for 4 h at 60 °C in a vacuum gas oven, considering the sensitivity of MXene, then directly implemented for electrochemical testing after cutting into 1 cm × 1 cm dimensions (Fig. 1). The mass loaded onto the PET substrate was precisely calculated to be 4.93 mg/cm^2.

2.10 Electrochemical measurements

An electrochemical workstation (WisEIS-1200 Premium) was used to conduct CV, GCD, and EIS of MXene, MnO_2@MXene, MXene/AgNWs, and MnO_2@MXene/AgNWs.

Additionally, the scan-rate test was conducted at scan rates from 20 to 100 mV s^{-1}, while GCD studies were conducted at current densities ranging from 0.5 to 4 A g^{-1}, and EIS analysis was performed in the frequency range of 10 Hz to 100 kHz. Electrochemical measurements were conducted using 3 M sulfuric acid as the electrolyte, silver/silver chloride as the reference electrode, and a platinum wire as the counter electrode. The fabricated MXene, MnO_2@MXene, MXene/AgNWs, and MnO_2@MXene/AgNWs were employed as working electrodes to evaluate their electrochemical responses. The specific capacitance, energy density, and power density of the fabricated materials were calculated as follows:

$$C_{sp} = \frac{Area}{2 \times \Delta V \times m \times scan\,rate} \quad (1)$$

$$C_{sp} = \frac{I \times \Delta t}{\Delta V \times m} \quad (2)$$

$$E = \frac{1}{2} CV^2 \quad (3)$$

$$P = \frac{E}{\Delta t} \quad (4)$$

where C_{sp} (F g^{-1}) is the specific capacitance that can be calculated from CV and GCD data, V is the potential window, and scan rate (mV s^{-1}). I (mA) represents the current at which the GCD was run, t (s) is the discharge time, and m (g) is the mass loaded. E (Wh/kg) is the energy density, and P (W/kg) is the power density, which can be calculated using Eqs. 3 and 4.

2.11 Characterization

Physiochemical characterizations of MXene, MXene/AgNWs, MnO_2@MXene, and MnO_2@MXene/AgNWs were conducted using XRD (BRUKER, D8 ADVANCE, South Korea), FE-SEM/EDS (SUPRA40VP, South Korea), and HR-TEM (JEM-ARM200F). Fourier transform infrared (FT-IR) spectroscopy (Perkin Elmer, Frontier, South Korea) and High-performance 3D imaging Raman spectroscopy (NANOPHOTON, RAMAN TOUCH, South Korea) were employed to analyze the nature of the functional groups and structural defects. A specific surface area analyzer (Micromeritics, ASAP24600, South Korea) was employed for surface area measurement. All characterizations were performed at the Center of University-Wide Range Research Facilities (CURF) at Jeonbuk National University in South Korea. Valence oxidation state analysis was performed using a hybrid XPS system (CJ115, South Korea) at the KBSI Center, Jeonbuk National University, Republic of Korea.

3 Results and discussion

3.1 Physical and chemical characterization

The combination of 0D@2D/1D active materials with synergistic effect, due to the presence of nanomaterials with different dimensions, was characterized by various structural and morphological techniques, including X-ray diffraction (XRD), FT-IR, Raman, BET, FE-SEM, EDS, and HR-TEM. Firstly, the MAX, MXene, MnO_2@MXene, MXene/AgNWs, and MnO_2@MXene/AgNWs were evaluated by XRD (Fig. 2a-b**)**. Figure 2a shows the XRD pattern of the MAX phase containing Miller indices (004), (101), (103), (105), (107), and (109) with high intensities. These high intensities were attributed to the presence of metallic Al in the MAX phase [27, 31]. The (002) plane could be assigned to the Ti–C bond. The observed peak at ~25° can be attributed to anatase TiO_2, indicating minor surface oxidation of MXene. However, the low intensity of this TiO_2 peak suggests that only a small fraction of MXene was oxidized, which is commonly observed under aqueous synthesis and processing conditions. The lattice spacing formula ($d = n\lambda/2\sin\theta$) was employed to calculate the interlayer distance. The c-lattice parameter for the MAX phase was calculated to be 12.48 Å, which can be attributed to the existence of a strong metallic bond between aluminum and titanium. After etching the Al layer, the diffraction peak associated with the aluminum middle layer disappeared in the XRD pattern of the etched MXene. Subsequently, the (002)-plane shifted from 9.8° (MAX phase) to 6.91°, demonstrating an increased interlayer spacing between the MXene sheets. The observation was supported by the calculated c-lattice parameter, which is 25.82 Å in the case of MXene. Low aluminum peak intensities, shifting of the (002) plane towards a lower angle, and increased c-lattice parameters indicate the removal of aluminum from the MAX phase, resulting in well-delaminated MXene galleries. The XRD pattern of MnO_2@MXene shown in Fig. 2b contains the (100), (110), (113), and (321) diffraction peaks of MnO_2 validating the successful anchoring of MnO_2 on the MXene surfaces. The slight shift of the (002) plane from 6.91° (MXene) to 6.10° (MnO_2@MXene) provide strong evidence to demonstrate the interaction between MnO_2 and MXene surface functional groups, rather than the intercalation of large MnO_2 particles (~25 nm) into the sub-nanometer interlayer galleries (~2.6 nm). Instead, the MnO_2 particles mainly were deposited at the surfaces and edges of the MXene sheets, which could prevent the macroscopic agglomeration of MXene

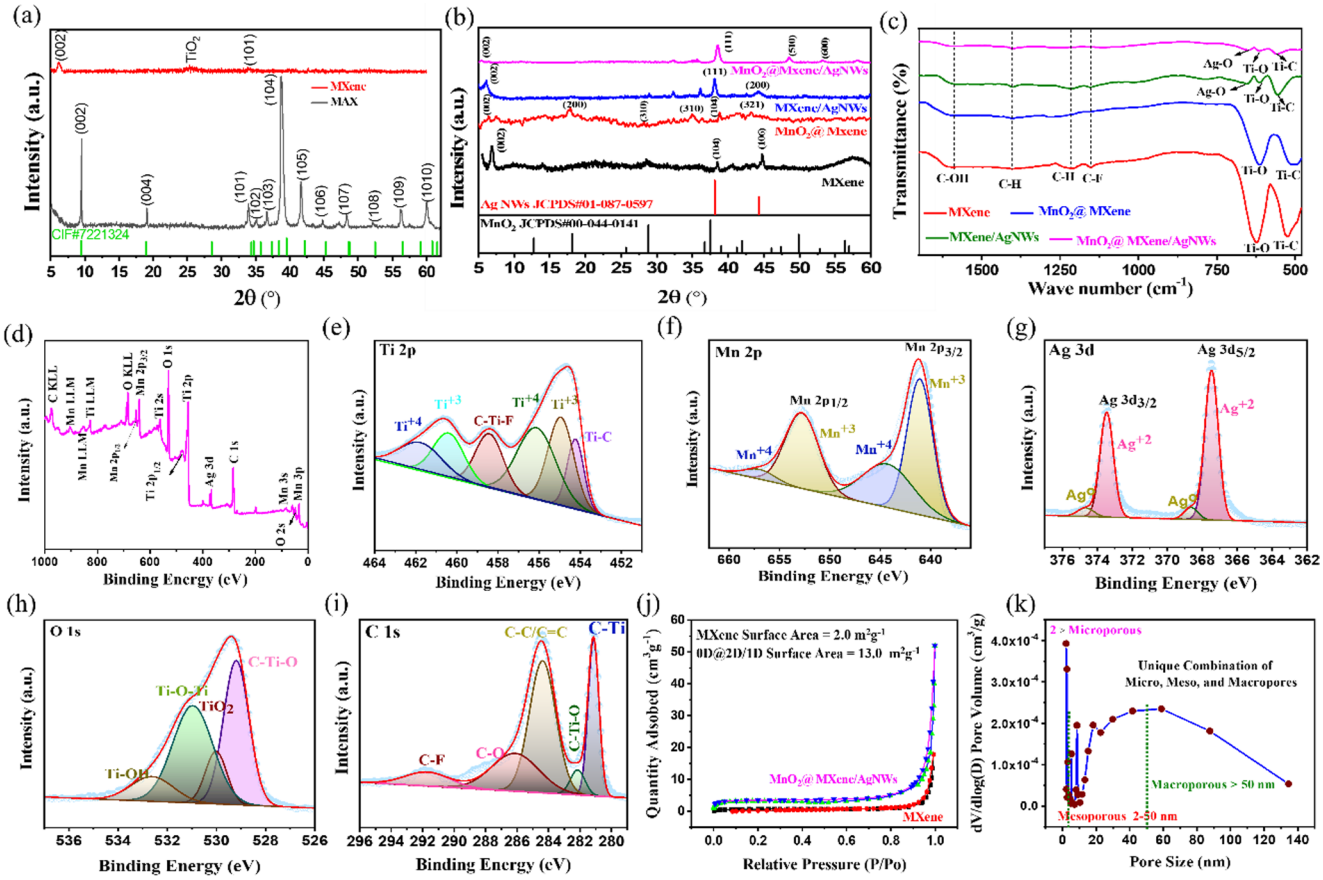


Fig. 2 XRD pattern of MAX, MXene, MnO_2@MXene, MXene/AgNWs, and MnO_2@MXene/AgNWs (**a**, **b**), FT-IR spectrum of MXene, MnO_2@MXene, MXene/AgNWs, and MnO_2@MXene/AgNWs (**c**); XPS analysis of MnO_2@MXene/AgNWs with survey spectrum (**d**), Ti 2p (**e**), Mn 2p (**f**), Ag 3 d (**g**), O 1 s (**h**), C 1 s (**i**), and BET analysis consisting of (**j**) a comparison of the surface areas of MXene and MnO₂@MXene/AgNWs, and (**k**) the pore-size distribution of the final composite

flakes and effectively inhibit the restacking of the MXene sheet. Similarly, the XRD pattern of the MXene/AgNWs exhibited the (002) diffraction peak of MXene at 5.93° and the (111) and (220) diffraction peaks at 38.08° and 44.4°, respectively. The observed peaks indicated the presence of AgNWs in the MXene host. Similar to MnO_2, the addition of AgNWs also contributes to the increase of interlayer spacing of the MXene layers, as evidenced by the shift of (002) plane from 6.91° (MXene) to 5.93° (MXene/AgNWs) and the enlarged c-lattice parameter of 25 Å. Finally, the XRD pattern of MnO_2@MXene/AgNWs contains the characteristic (002) diffraction peak of MXene, and the (111) and (200) diffraction peaks confirm the presence of AgNWs in the synthesized composite material. However, the composite exhibited (113) and (111) MnO_2 planes, which can be attributed to the presence of MnO_2 along with AgNWs. The shift in the (002) plane from 6.10° to 5.51° further indicates the increase of the interlayer spacing of MXene, resulting from the physical support of AgNWs and MnO_2 between the MXene layers. One-dimensional AgNWs are available for physical support to MXene sheets, like MnO_2. Therefore, the final sample exhibits a large peak shift and a high c-lattice parameter (28.62 Å), as shown in Fig. 2b. The results obtained confirm the physical support provided by MnO_2 and AgNWs in the MXene host, which can enhance the chemical and mechanical stability of MXene. Moreover, the characteristic XRD spectrum of MnO_2 and AgNWs is provided in Figure S2a and Figure S2b, to validate the synthesis of MnO_2 and AgNWs, respectively.

FT-IR spectroscopy was employed to characterize the functional groups on the surfaces of the as-synthesized materials, as illustrated in Fig. 2c. The FT-IR spectrum of MXene was recorded in the range of 1700–400 cm^{-1}, where the peaks at 523 and 624 cm^{-1} could be attributed to the Ti–C and Ti–O bands [31, 32]. Similarly, the peaks at 1151, 1212, 1394, and 1610 cm^{-1} can be attributed to the C–F, C–H, C–H, and C–OH bands, respectively, which are consistent across all samples with minimal differences in peak intensities. The FT-IR spectrum of MnO_2@MXene exhibited both Ti–C and Ti–O bands, analogous to those of MXene. Furthermore, the FT-IR spectrum of the MXene/AgNWs exhibited peaks similar to those of MXene, with

one additional peak at 655 cm^{-1}, which can be attributed to Ag–O bond vibrations [32, 33]. Finally, MnO_2@MXene/AgNWs exhibited Ti–C, Ti–O, Ag–O, C–F, C–H, and C–OH peaks, like those of the MXene and MXene/AgNWs samples. The MXene surface is well-terminated with F, O, and OH functional groups, which are advantageous for charge-storage applications, especially in acidic electrolytes. Additionally, Raman spectroscopy is shown in Figure S3 and briefly discussed to investigate structural defects in MXene and MnO_2@MXene/AgNWs.

To elucidate the surface chemistry of MnO_2@MXene/AgNWs, XPS analysis was conducted, and the peaks were deconvoluted, as shown in Fig. 2d-i. The survey spectrum exhibited all the characteristic peaks of the Ti, C, O, Mn, and AgNWs (Fig. 2d). Notably, peaks at binding energy of 33.64, 48.15, 83.17, 283.41, 376.96, 455.29, 477.88, 530.18, 560.82, 640.78, 652.76, 685.25, 825.11, 852.99, 902.53, and 972.35 eV can be assigned to Mn 3p, O 2 s, Mn 3 s, C 1 s, Ag 3 d, Ti 2p, Ti $2p_{1/2}$, O 1 s, Ti 2 s, Mn $2p_{3/2}$, Mn $2p_{1/2}$, O KLL, Ti LLM, Mn LLM, Mn LLM, and C KLL, respectively [33, 34],. The high-resolution Ti 2p spectrum shown in Fig. 2e was deconvoluted into Ti-C (454.25 eV), Ti^{3+} (454.97, 460.6 eV), Ti^{4+} (456.18, 461.9 eV), and C–Ti–F (458.44 eV) peaks. It has been reported that Ti–C signals originate from the interior of the MXene layers [34, 35]. Similarly, Fig. 2f showed the deconvoluted spectrum of Mn 2p into Mn^{3+} (641.08, 652.76 eV) and Mn^{4+} (644.59, 657.33 eV), validating the presence of MnO_2 in the desired oxidation states in the final synthesized composite. However, the oxygen-rich termination of MXene sheets and MnO_2 incorporation compromise the conductivity of MXene, which makes the addition of conductive AgNWs beneficial for the high capacity and fast charging. After adding AgNWs, their presence can be confirmed from the high-resolution spectrum of Ag 3d. The peaks in Fig. 2g were deconvoluted into high-resolution Ag^0 (368.65, 374.6 eV) and Ag^{2+} (367.49, 373.44 eV) oxidation states, respectively [36]. Similarly, the high-resolution spectra of O 1 s presented in Fig. 2h indicate the deconvoluted signals of C–Ti–O, TiO_2, Ti–O–Ti, and Ti–OH at 529.14, 529.96, 530.95, and 532.6 eV, respectively, confirming the presence of O and OH groups at the surface of MXene, which is highly favorable for charge storage in acidic electrolyte (H^+). Furthermore, the high-resolution spectra of C 1 s presented in Fig. 2i exhibit signals at 281.1, 282.13, 284.28, 286.13, and 291.17 eV, which can be ascribed to the C–Ti, C–Ti–O, C–C/C = C, C–O, and C-F bonds, respectively [35, 37]. In summary, the XPS spectrum elucidates the surface composition of MXene, demonstrating surface termination with oxygen– and hydroxyl–rich functionalities, as well as the presence of Mn and AgNWs in the resulting sample. The proposed interaction between all three constituents is presented in Figure S4.

The BET nitrogen adsorption-desorption isotherms of MXene and MnO_2@MXene/AgNWs are presented in Fig. 2j–k. Figure 2j shows that the isotherms were classified as type IV based on the IUPAC classification, which suggests the porous nature of the materials [22]. The BET surface area of MXene was calculated to be 2.0 $m^2\ g^{-1}$. However, the BET surface area of MnO_2@MXene/AgNWs is 13.0 $m^2\ g^{-1}$, which is 6.5 times higher than that of the pure MXene. The higher surface area of the final composite can be attributed to the decoration and physical barrier of MnO_2 nanoparticles between MXene sheets, which reduces the restacking of the MXene sheets and results in a high surface area and active sites for electrolyte interactions. BJH pore size distribution plot for the final composite displays (Fig. 2k) the existence of a broad range of pore sizes, including the micropores (pore diameter < 2 nm), mesopores (50 nm > pore diameter > 2 nm), and macropores (pore size > 50 nm) [38]. This synergistic combination of micro, meso, and macro-sized pores is highly responsible for the enhanced surface area, which can facilitate the storage of many electrolyte ions during charging and less resistive discharging due to the wide range of pore diameters. The pore volumes of the fabricated materials exhibit a satisfactory value of 0.004284 cm^3/g.

FE-SEM analysis was conducted to evaluate the morphological changes in the synthesized materials during etching, delamination, decoration, and composite synthesis, as displayed in Fig. 3. Figure 3a shows the MAX phase with extremely tightly packed layers, which can be attributed to the strong metallic bonding between titanium and aluminum. However, Fig. 3b shows well-delaminated MXene layers following the removal of Al, resulting in a continuous gap between the MXene flakes. This enhanced interlayer gap provides numerous accessible sites for electrolyte ions. Nevertheless, functionalized MXene sheets exhibit Van Der Waals forces responsible for the restacking of the sheets and reduced interlayer gap.

Consequently, the 0D-MnO_2 NPs were synthesized and decorated on MXene sheets. These particles act as spacers between the MXene bundles to inhibit self-aggregation and provide excessive charge storage sites, as shown in Fig. 3c. The FE-SEM micrographs for MnO_2@MXene provide clear evidence of the decoration of MnO_2 NPs on the MXene sheets, which is responsible for maintaining the accessible surface area. Similarly, FE-SEM micrographs of the final composite MnO_2@MXene/AgNWs **(**Fig. 3d**)** illustrate the successful decoration of MnO_2 and AgNWs on MXene sheets, which is highly responsible for preserving the porous architecture and preventing the self-stacking of MXene bundles through steric hindrance. Additionally, electrostatically joined (van der Waals forces) AgNWs on the MXene sheets enhance the conductivity and simultaneously increase the

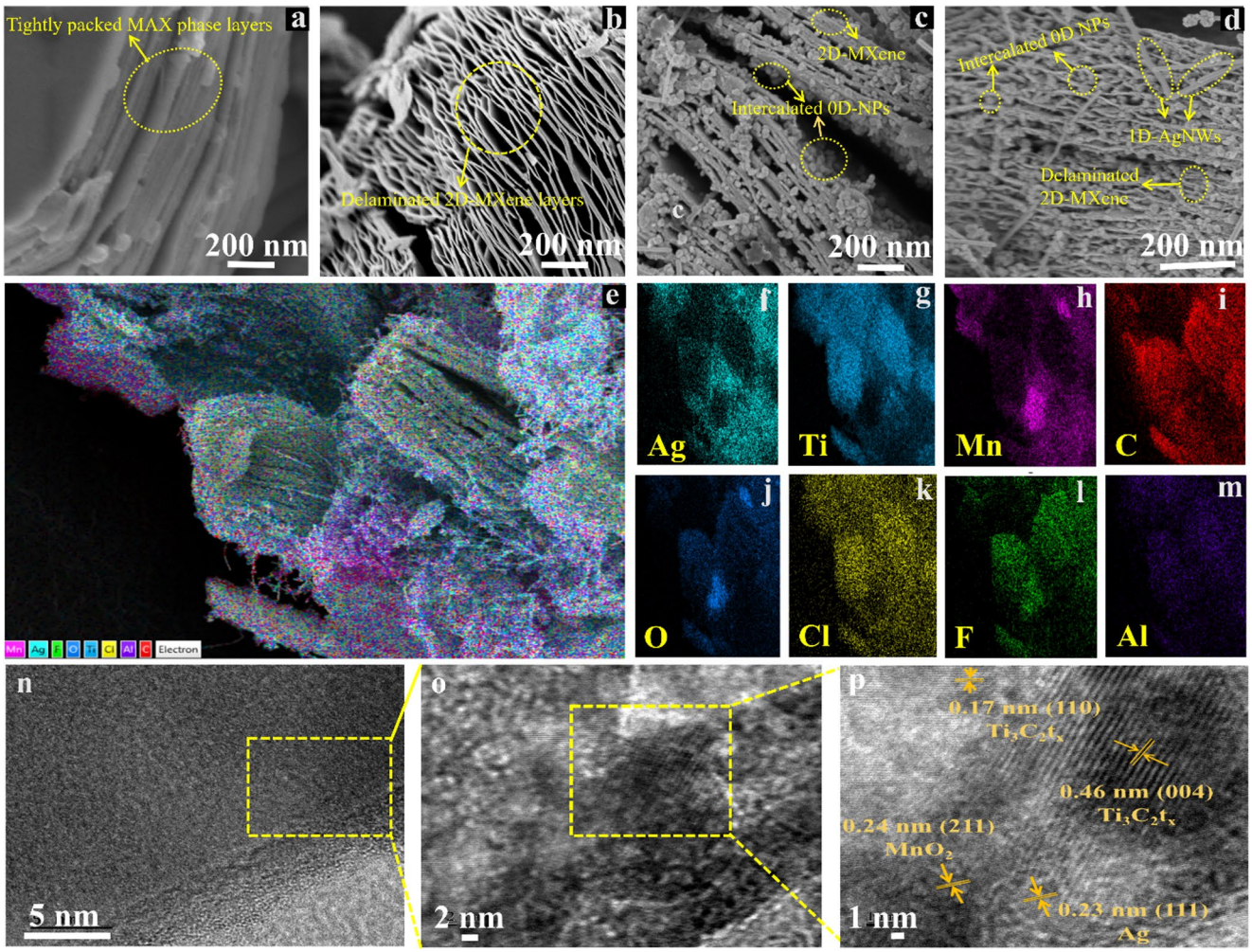


Fig. 3 FE-SEM images of (**a**) MAX phase, (**b**) MXene, (**c**) MnO_2@MXene, and (**d**) MnO_2@MXene/AgNWs; (**e-m**) color mapping of MnO_2@MXene/AgNWs; HR-TEM images (**n-p**) at various resolutions for in-depth morphological analysis

number of active sites. The FE-SEM micrograph for MnO_2 and AgNWs is displayed in Figures S5 and S6 to elucidate their specifically designed 0D and 1D morphologies. In summary, the strategy of in combination of MXene sheets with the 0D MnO_2 and 1D AgNWs helps to reduce restacking, increase the accessible active sites for electrolyte ions, and increase surface area, which are key parameters for achieving high electrochemical storage performance. Additionally, the morphological analysis confirms the formation of three different morphological (OD-MnO_2, 1D-AgNWs, and 2D-MXene sheets) synergies: 0D@2D/1D.

EDS analysis and color mapping of the final modified composite (MnO_2@MXene/AgNWs) were conducted to analyze the elemental composition and dispersion of MnO_2 and AgNWs on the MXene sheets, as shown in Fig. 3e-m. The resulting color mapping provides a clear indication that Ag, O, and F are dispersed on the MXene sheets, Mn is present between the MXene sheets, and Ti and C represent the elemental components of the MXene sheets. The EDS spectrum of the final sample is shown in Figure S7 and illustrates the elemental compositions of the synthesized materials. The spectrum exhibited a high intensity for Ti, C, and O along with the low-intensity peaks of Mn, Ag, F, Cl, and Al, confirming that the composite contained all the elements of interest in the desired quantities. Aluminum exists in the form of Al_2O_3 (0.19 wt%), which can be considered negligible and indicates the successful removal of Al. The results obtained are consistent with the XRD, XPS, and FE-SEM results, which suggest that the final composite contains both Mn and AgNWs in the MXene galleries, with negligible amounts of Al remaining.

In-depth analysis of the morphology and microstructure of MnO_2@MXene/AgNWs was conducted through HR-TEM analysis, as shown in Fig. 3n–p. Initially, at 5 nm, it was difficult to find the lattice fringes. Therefore, the selected portion was zoomed to 2 nm and 1 nm, respectively, where the lattice fringes of MXene, MnO_2, and AgNWs can be easily depicted. Additionally, Fig. 3p illustrates the fringes spacing

of 0.17, 0.46 nm, 0.23, and 0.24 nm, at the corresponding planes of (110), (004), (111), and (211), which can be attributed to the $Ti_3C_2T_x$, AgNWs, and MnO_2, respectively. The existence of fringes spacing of 0.17 and 0.46 nm ensures the synthesis of MXene, and fringes spacing of 0.23 nm and 0.24 nm confirms the presence of MnO_2 and AgNWs in the final composite (MnO_2@MXene/AgNWs).

3.2 Electrochemical three-electrode system testing

A three-electrode system was employed to evaluate the electrochemical performance of MXene, MnO_2@MXene, MXene/AgNWs, and MnO_2@MXene/AgNWs. This research work aims to comprehensively understand the effect of 0D-MnO_2 NPs decoration and the subsequent addition of 1D-conductive AgNWs to a 2D-MXene sheet gallery on the relationship between structure and the charge-storage capability of the as-synthesized 0D@2D/1D composite. All electrochemical tests were conducted in a 3 M aqueous H_2SO_4 solution with a Pt wire as the counter electrode and silver chloride as the reference electrode. Furthermore, electrochemical characterizations such as cyclic voltammetry (CV), galvanostatic charge–discharge (GCD), and electrochemical impedance spectroscopy (EIS) analyses were carried out to determine the impact of 0D-MnO_2 and 1D-AgNWs synergy on the capacitive behavior of 2D-MXene sheets, as displayed in Fig. 4. Initially, CV analysis was performed in the optimized potential range of 0 to 0.4 V for MXene, MnO_2@MXene, MXene/AgNWs, and MnO_2@MXene/AgNWs at 30 mV s^{-1}, as shown in Fig. 4a. It is worth noting that previous studies have reported a relatively wide potential window (e.g., −0.35 to 0.4 V) for MXene electrodes in acidic electrolytes [39, 40]. However, the optimal operating range strongly depends on electrode composition and interfacial stability. In this study, the potential window was determined based on GCD-based optimization (Figure S8 and Sect. 3, Supporting Information). Briefly, compared with the extended

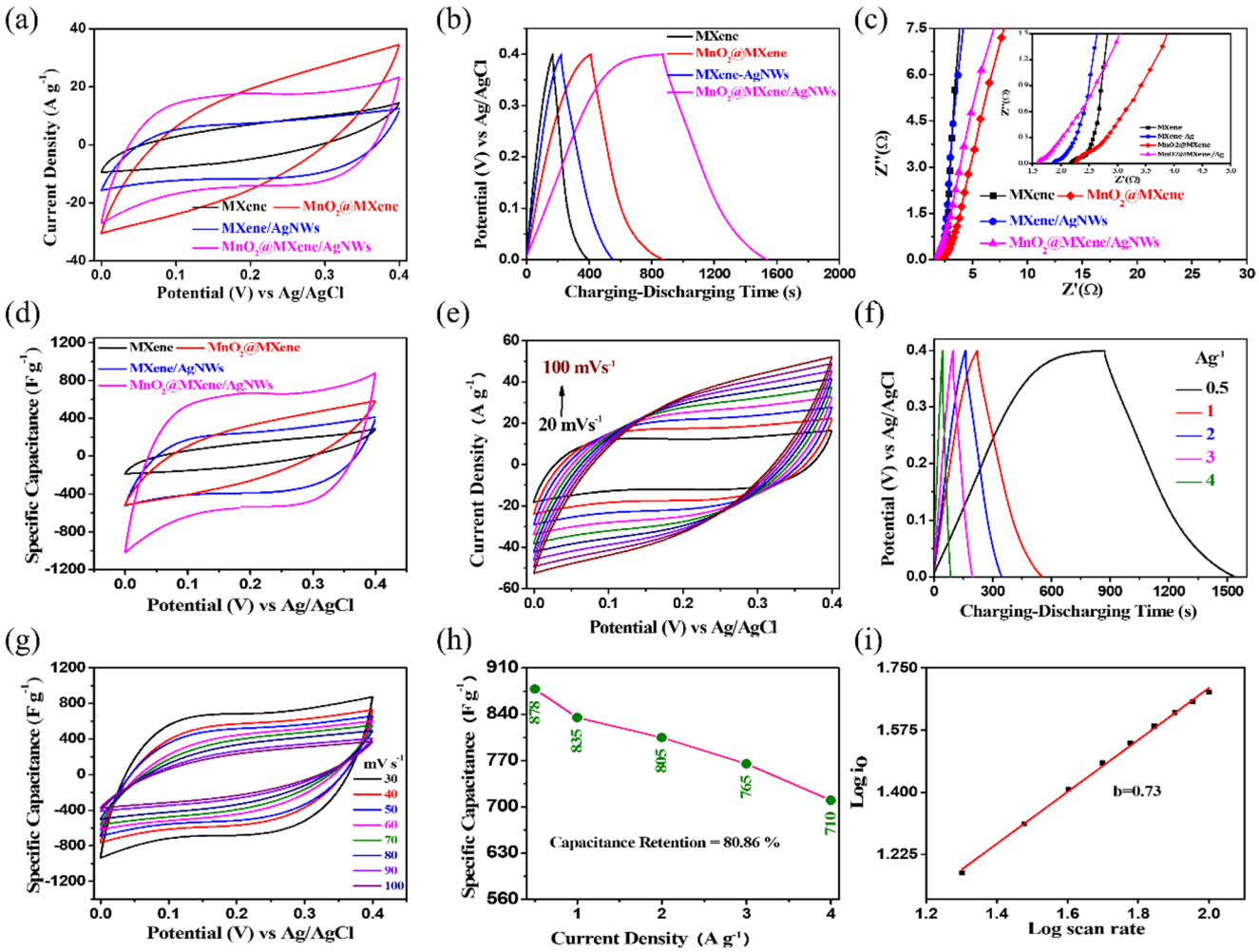


Fig. 4 CV (**a**), GCD (**b**), and EIS (**c**) behavior of MXene, MnO_2@MXene, MXene/AgNWs, and MnO_2@MXene/AgNWs. Capacitance comparison of all samples (**d**); effect of scan rate from 20 to 100 mV s^{-1} (**e**), current density from 0.5 to 4 A g^{-1} (**f**), capacitance in F g^{-1} from scan rate (**g**), current density (**h**), and b value for the final fabricated material MnO_2@MXene/AgNWs (**i**)

potential window of −0.1–0.5 V, the 0–0.4 V range showed a smaller potential drop and a more stable charge–discharge profile, indicating lower polarization and better electrochemical reversibility for the MnO_2@MXene/AgNWs composite electrode. Therefore, this optimized potential range was used for subsequent electrochemical measurements. The MXene/AgNWs composite exhibited an increased current density and peak area compared with the pure MXene electrode, indicating that the addition of AgNWs enhances the electrochemical performance of MXene by providing additional conductive channels. Although the subsequent addition of AgNWs improves the performance of MXene, it still demonstrates lower capacitive current values, which can be attributed to the partial incorporation of AgNWs in the MXene sheets, resulting in the restacking of the MXene sheets and consequently reducing the number of available active sites for charge storage.

To address this issue, 0D pseudo-MnO_2 NPs were decorated on MXene sheets, providing a significantly larger peak area and higher current density due to their (1) contribution to charge storage, (2) functioning as active redox sites, and (3) preventing the agglomeration of MXene layers. The decoration of MnO_2 increases the capacitance of MXene. Thus, the final composite (MnO_2@MXene/AgNWs) was optimized, which combined the synergy of the MnO_2 and AgNWs conductivity to enhance the energy storage application of MXene. The obtained results exhibit excellent CV curves with perfect rectangular shapes and high capacitive current density, which can be attributed to the more conductive channels formed by the AgNWs and reduced restacking of the MXene layers through MnO_2 decoration. Moreover, the large CV area and current density can be attributed to the synergy (OD-MnO_2, 1D-AgNWs, and 2D-MXene sheets) of the three different morphological materials, supporting pseudocapacitive charge storage. The rectangular CV curve for the final composite is consistent with previously reported supercapacitor results [41], and the electrochemical performance is comparable to other MnO_2@MXene based systems listed in Table S1.

GCD analysis was conducted for all four fabricated materials. As shown in Fig. 4b, the final optimized MnO_2@MXene/AgNWs exhibited the largest charge-discharge time (1552 s) at the same current density (0.5 A g^{-1}), which can be attributed to the synergistic effect of the 0D-MnO_2, 1D-AgNWs, and 2D-MXene layers. A slight asymmetry in the charge–discharge profile is also observed at this low current density, which is commonly seen in pseudocapacitive systems and can be attributed to polarization and ion-transport limitations. In contrast, the other three samples exhibited lower charging-discharging time compared to the final composite, which can be attributed to the sum of advantages provided by each constituent of the composite. Notably, the charge–discharge profiles become more symmetric at higher current densities (Fig. 4f), indicating more balanced electrochemical behavior under practical operating conditions. This observation suggests that further optimization of MnO_2 distribution, conductive pathways, and ion diffusion channels could help reduce polarization and improve charge–discharge symmetry. Furthermore, the GCD results corroborate the CV results, excellent current density, pseudocapacitive charge storage, and high charging-discharging time, rendering MnO_2@MXene/AgNWs a promising candidate for applications in the field of energy storage.

Furthermore, EIS analysis was performed to assess the charge-transfer resistance (R_{ct}) and ion-transfer resistance of those four electrodes, as shown in Fig. 4c. All four samples possessed small semicircle diameters. The MXene/AgNWs and MnO_2@MXene show the smallest and largest diameters, respectively. The MnO_2@MXene shows the largest charge transfer resistance, which may be due to the presence of MnO_2, which blocks the channels due to the presence of the 0D particles and reduced conductivity. However, the addition of MnO_2 is beneficial for preventing the stacking of the MXene layers. In contrast, the MnO_2@MXene/AgNWs exhibited a smaller semicircle diameter owing to the presence of highly conductive 1D-AgNWs channels. The charge transfer resistance (R_{ct}) values for all samples were calculated to be 2.8, 2.5, 2.2, and 1.8 Ω for MnO_2@MXene, MXene, MnO_2@MXene/AgNWs, and MXene/AgNWs, respectively.

MnO_2@MXene/AgNWs demonstrated the highest capacitance (878 F g^{-1}) among all four samples, owing to their high current density, discharge time, and low R_{ct} value (2.2). MXene, MXene/AgNWs, and MnO_2@MXene exhibited specific capacitances of 285, 411, and 582 F g^{-1}, respectively, as shown in Fig. 4d. MnO_2@MXene/AgNWs contains 1D-AgNWs and 2D-MXene layers, which is beneficial for their application as a flexible supercapacitor, while 0D-MnO_2 facilitates the achievement of high packing density, which is crucial for obtaining high areal capacitance and cyclic stability. Additionally, the composite exhibited electrostatic interactions, which provided stable integrity to the composite and motivated the utilization of MnO_2@MXene/AgNWs for further electrochemical studies, such as the effect of different potentials, GCD at various current densities, and device fabrication. Figure 4e illustrates the CV curves of MnO_2@MXene/AgNWs under different scan rates from 20 to100 mV s^{-1}. The current density increases linearly with the increase of the scan rates, which demonstrates the fast-charging feature of the materials due to the high driving force on the charges at a high scan rate to accommodate their sites on the electrode surface. The CV curves maintained their rectangular shapes with increased scan rate, suggesting a stable and reversible electrochemical

reaction. Similarly, Figure S9 illustrates the impact of different scan rate on the current density values for MXene (Figure S9a), MnO_2@MXene (Figure S9b), and MXene/AgNWs (Figure S9c), respectively, and also discussed in details in SI.

Moreover, to quantify the impact of different current densities on the specific capacitance of MnO_2@MXene/AgNWs, the GCD measurements were carried out at various current densities ranging from 0.5 to 4 A g^{-1} with the material loading of 5 mg cm^{-2}, as shown in Fig. 4f. At all current densities, the charging and discharging curves maintain their shapes, verifying the stable performance of the MnO_2@MXene/AgNWs material at various input current densities. However, at a low current density (0.5 A g^{-1}), the shape of the CV curve starts to transition from EDLC to resistive, indicating the minimum potential current density for the material. Discharge durations of 41, 110, 189, 305, and 727 s were observed at current densities of 4, 3, 2, 1, and 0.5 A g^{-1}, respectively. At high current densities, the reduced discharge time can be attributed to rapid storage due to insufficient time for the charges to occupy the active sites on the material surface. Furthermore, the specific capacitance values were calculated at various scan rates based on the CV curve areas, as shown in Fig. 4g. Capacitance values of 841, 805, 746, 706, and 665 F g^{-1} were obtained at scan rates of 30, 40, 60, 80, and 100 mV s^{-1}. The decrease in the capacitance at higher potentials can be attributed to rapid potential sweeping, which provides insufficient time for ion storage within the layers; consequently, only surface-level charge storage contributes to the reduced capacitance. Similarly, the GCD profiles at various current densities were also utilized to calculate the specific capacitance values, as displayed in Fig. 4h, which were comparable to the values calculated from various CV. The calculated specific capacitances at current densities of 4, 3, 2, 1, and 0.5 A g^{-1} are 709, 764, 807, 834, and 878 F g^{-1}, respectively. The highest capacitance values at low current densities were attributed to slow charging, which facilitates charge accommodation at all possible sites on the fabricated material surface. The fabricated material exhibited stable capacitance values at various current densities, indicating its potential for practical applications. Additionally, a supplemented graph was plotted between the log current (log i_0) and log scan rate at scan rates of 20, 40, 60, 80, and 100 mV s^{-1}, and the slope of the obtained graph was calculated from Fig. 4i, with a b value of 0.73. A b value of 1 indicates ideal capacitive behavior, while 0.5 signifies ideal diffusion-controlled behavior [42]. The obtained slope value (b = 0.73) lies between the ideal capacitive and diffusion-controlled values, suggesting the involvement of both charge storage mechanisms in the fabricated material. MXene, a 2D base material, comprises a high proportion of carbon that facilitates surface-assisted charge storage, whereas MnO_2 and AgNWs contribute to diffusion-controlled charge storage, resulting in the material exhibiting a diffusion-controlled mechanism. Additionally, two fabricated electrodes with a lower concentration of MnO_2 (2.5 mg) in the final composite (MnO_2@MXene/AgNWs) are probably responsible for little aggregation and an optimized concentration of MnO_2 (5 mg). The cyclic voltammetry and GCD comparison are provided in Figure S10, where the optimized MnO_2 value exhibits higher current density and GCD time. MnO_2 plays a key role in charge storage by utilizing the oxidation-redox cycle. A lower concentration of MnO_2 will lower the extent of redox reaction and ultimately the overall capacitance of the fabricated material.

Moreover, to examine the effect of the scan rate on the percentage contribution of charge storage, Dunn's real method was employed. Figure S11a presents a bar graph illustrating the percentage contributions of capacitive and diffusion-controlled charge storage at various potentials in the range of 20–100 mV s^{-1}. Furthermore, to investigate whether the fabricated material possessed a reversible charge storage mechanism, the scan rate and anodic-cathodic current values were plotted. Figure S11b demonstrates 0.97 and 0.96 R^2 values for anodic and cathodic current, respectively, indicating that the fabricated material is responsible for reverse charging. Additionally, Dunn's real graph was constructed to provide a comprehensive representation of the percentage contributions at various potentials, as illustrated in Figure S11c-k. At 20 mV s^{-1}, the material exhibits 65.8% diffusion-controlled and 34.2% capacitive-controlled charge storage (Figure S11c). Similarly, with increasing scan rate, the contribution of the capacitive-controlled charge storage mechanism increases. At higher potentials, such as 70 and 80 mV s^{-1}, the charge storage contributions of diffusion-controlled and capacitive-controlled mechanisms were approximately equivalent (50% each) (Figure S11h-i). At 90 and 100 mV s^{-1}, the capacitive-controlled mechanism contributed 52.4% and 53.7% (Figure S11j, k), respectively, dominating the diffusion-controlled mechanism. The decrease in the diffusion–controlled charge storage contribution at higher scan rates can be attributed to the limited time available for charge diffusion inside the material surface, resulting in charge storage solely on the electrode surface. The obtained results are highly consistent with the observation that the MnO_2@MXene/AgNWs composite with three different morphologies (0D-MnO_2, 1D-AgNWs, and 2D-MXene) demonstrates extensive charge storage capability, supporting its utility in practical applications. The final MnO_2@MXene/AgNWs composite was utilized to fabricate a flexible and printable ASC device to communicate its practical utility.

The viscosity and thixotropic behaviors of the as-prepared inks were initially evaluated to determine their suitability for fabricating printing devices. The AC and MnO_2@MXene/AgNWs inks exhibited pronounced shear-thinning behavior, a non-Newtonian characteristic, where the viscosity decreased with increasing shear rate. Specifically, the viscosities of these inks (Fig. 5a, c) decrease significantly, from 41,800 cP to 210 cP and from 8,000 cP to 85 cP, over shear rate ranges of 0–450 s^{-1} and 0–250 s^{-1}, respectively. This substantial reduction in viscosity under shear facilitated a smooth flow through the syringe nozzle, enabling efficient application under pressure. Upon removal of the shear forces, the inks regained their initial high viscosity, which enhanced the stability and precision of the printed patterns. Both inks also demonstrated thixotropic behavior, characterized by a temporary reduction in viscosity under shear stress and subsequent recovery upon stress removal. Cyclic shear tests (Fig. 5b, d) highlighted this thixotropic recovery, which is a critical property for high-resolution printing. Rapid recovery minimizes unintended spread or smudging after application, ensuring well-defined pattern edges. This behavior is particularly advantageous for applications requiring high precision, as it prevents ink flow or dripping after deposition. These rheological properties enable the formation of precise, stable, and accurate electrode configurations, rendering the ink suitable for advanced printing applications. Finally, the effect of MnO_2 decoration on the chemical stability of MXene was examined through three-electrode stability analysis (Figure S12) and is discussed in the Supporting Information.

3.3 Electrochemical two-electrode system testing

To further investigate their practical application, ASC devices were fabricated using AC as the negative electrode and MnO_2@MXene/AgNWs as the positive electrode, as illustrated in Fig. 5e. In this device (MnO_2@MXene/AgNWs//AC), both the positive and negative electrodes were printed in a comb-like structure on a nonconductive polyethylene terephthalate (PET) substrate, and PVA+H_2SO_4 gel was used as the electrolyte, as shown in Fig. 5e. In order to show the printing resolution and size of electrodes, microscopic images are shown in Figure S13, showing a width and spacing between the lines of ~1900 and ~1352 µm, respectively. The charge-discharge mechanism of MnO_2@MXene/AgNWs in an acidic electrolyte is presented in Fig. 6a. The fabricated material was a combination of transition metal oxides (MnO_2 and Ag_2O) and MXene (Ti_3C_2O-H_xF_y). FT-IR and XPS analyses demonstrated the presence of oxygen-rich termination at the MXene sheets for example the Ti-O and Ti–OH entities. Initially, MnO_2, which possesses Mn in the (4+) oxidation state, undergoes a reduction during the charging process, wherein Mn^{4+} shifts to Mn^{3+} by accepting an electron and forming MnOOH in an acidic electrolyte that contains H^+ active ions available for storage. Conversely, the discharging process involves the oxidation of Mn^{3+} to Mn^{4+}, releasing an electron for use as electricity, as shown in the reaction in Fig. 6a and Figure S14a-b. These reactions indicate that MnO_2 is a highly favorable material for controlling the oxidation of MXene owing to its high capacity for oxidation and reduction reactions [43].

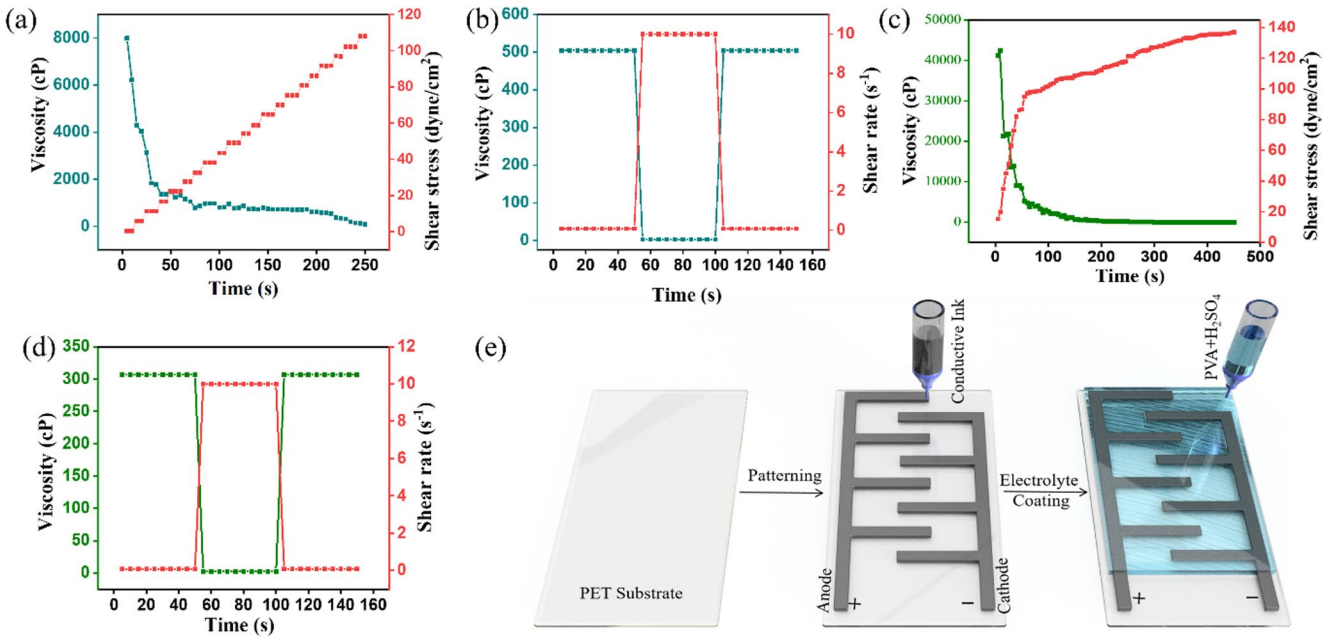


Fig. 5 Ink rheology and thixotropic recovery of the prepared MnO_2@MXene/AgNWs (**a**, **b**) and activated carbon (**c**, **d**) inks; (**e**) step-by-step fabrication and optical image of the flexible ASC device printed by DIW

Furthermore, the charge-discharge mechanism of AgNWs in the presence of an acidic electrolyte is also presented. Most significantly, the charge storage mechanism of oxygen-rich MXene is illustrated, which facilitates an understanding of the faradic-controlled charge storage contributions. In this context, Ti in the 4+oxidation state during charging was converted into 3+, which maximized the charge storage capacity of MXene. Conversely, discharging involves the retention of the original oxidation state by releasing the stored electrons. A summary of this data provides evidence that, during charging, electrolyte ions (H^+) undergo reduction and store electrons. During discharge, the electrolyte ions return to the original state by releasing electrons (e^-). These oxidation-reduction cycles can compromise the stability of MXene; however, the presence of MnO_2 can mitigate this problem by providing chemical and mechanical stability to MXene, acting as a chemical stabilizer against oxidation and a highly reactive species for redox reactions. Similarly, the EDLC charge-storage mechanism is illustrated in Fig. 6b, which is attributed to electrostatic ion adsorption at the accessible electrode–electrolyte interface, facilitated by the high surface area, conductive pathways, and open architecture of the composite.

The mechanical strength of the ASC is provided in Figure S15, having the ability to bear a 450 N force before breaking. The printed asymmetric device was operated at the following bending angles: 0, 30, 45, and 90 °. It can be depicted from Figure S16 that the device showed very little deviation in charging and discharging time at various bending angles, thanks to the stability of the material at various bending angles. Based on these charging-discharging cycles, the areal capacitance was compared by considering capacitance at 0 ° as standard (100%). The inset Figure S16 shows 98.8, 93.48, and 91.02% capacitance retention at 30, 45, and 90 ° bending of the designed device. The observed results clearly demonstrate the noticeable capacitance even at 90 ° bending, validating its applicability at various points where flexibility and mechanical stability are needed. The working cyclic voltammograms of the anode and cathode materials are displayed in Fig. 7a to analyze their performance in the negative and positive potential windows. Additionally, to optimize the working potential window of the ASC, GCD measurements were taken at various potential windows, such as −0.2 V to 0.6, 0.8, 1.0, 1.2, and 1.4 V at a current density of 6 mA cm^{-2}, respectively. As shown in Fig. 7b, the GCD measurements were taken with an increment of 0.2 V, and consistent results were observed without electrolyte decomposition and charge saturation. The final composite exhibits stable performance within a potential window of 1.6 V. For further confirmation of the working potential window, CV analysis was conducted at 50 mV s^{-1} in potential ranges of −0.2 V to 0.8, 1.0, 1.2, and 1.4 V, as illustrated in Fig. 7c. The device demonstrated consistent results without electrolytic decomposition for all potential sweeps. However, beyond this potential window, electrolytic decomposition and electrode oxidation occurred. Consequently, to ensure stable device performance, subsequent analyses were conducted within the optimized potential window of 1.6 V (−0.2 to 1.4 V). The stable working potential window of the fabricated material can be attributed to the controlled oxidation of the fabricated material through MnO_2-supported MXene. Moreover, Fig. 7d presents the CV curves of the device obtained at various scan rates ranging from 20 to 1000 mV s^{-1} within a constant potential window of −0.2 to 1.4 V.

The CV curves demonstrate that the ASC device exhibits hybrid supercapacitor-like behavior. Moreover, the CV curves maintain their characteristic shape, even at a high applied potential of 1000 mV s^{-1}. The observed behavior of the fabricated device indicates its durability, stability, and reversibility at high-potential sweeps. Similarly, Fig. 7e presents the GCD profiles of the ASC device at various applied current densities of 6, 8, 10, 12, and 14 mA cm^{-2} within the optimized potential window of −0.2 to 1.4 V. The quantity of charges stored on the material surface is dependent on the applied current density. At higher current densities, reduced charging and discharging times result in lower capacitance values, which can be attributed to the limited time available for the electrolyte ions to adsorb onto the material surface and diffuse inside the MXene layers, which is responsible for the low charge storage. The highest capacitance value was recorded as 565.1 mF cm^{-2} @ 6 mA cm^{-2}, which can be attributed to the sufficient time for the electrolyte ions to be stored on the surface and diffuse inside the layers, as illustrated in Fig. 7f. However, at current densities of 8, 10, 12, and 14 mA cm^{-2}, the areal capacitance decreased marginally to 424, 351.8, 318.0, and 307.1 mF cm^{-2}, respectively. The fabricated material exhibited notable areal capacitance, even at high current densities, and exhibited 54.3% capacitance retention at a current density of 14 mA cm^{-2}. The lower rate performance of the ASC device compared with the MnO_2@MXene/AgNWs electrode measured in the three-electrode system can be attributed to the difference between single-electrode evaluation and full-device operation. In the three-electrode configuration, the measured capacitance mainly reflects the intrinsic electrochemical behavior of the MnO_2@MXene/AgNWs electrode, whereas the ASC device performance is affected by the combined behavior of both positive and negative electrodes, charge balance, interfacial/contact resistance, electrolyte accessibility, ion diffusion across the full cell, and polarization at high current densities. Therefore, although the MnO_2@MXene/AgNWs electrode shows good rate capability in the three-electrode system, the assembled

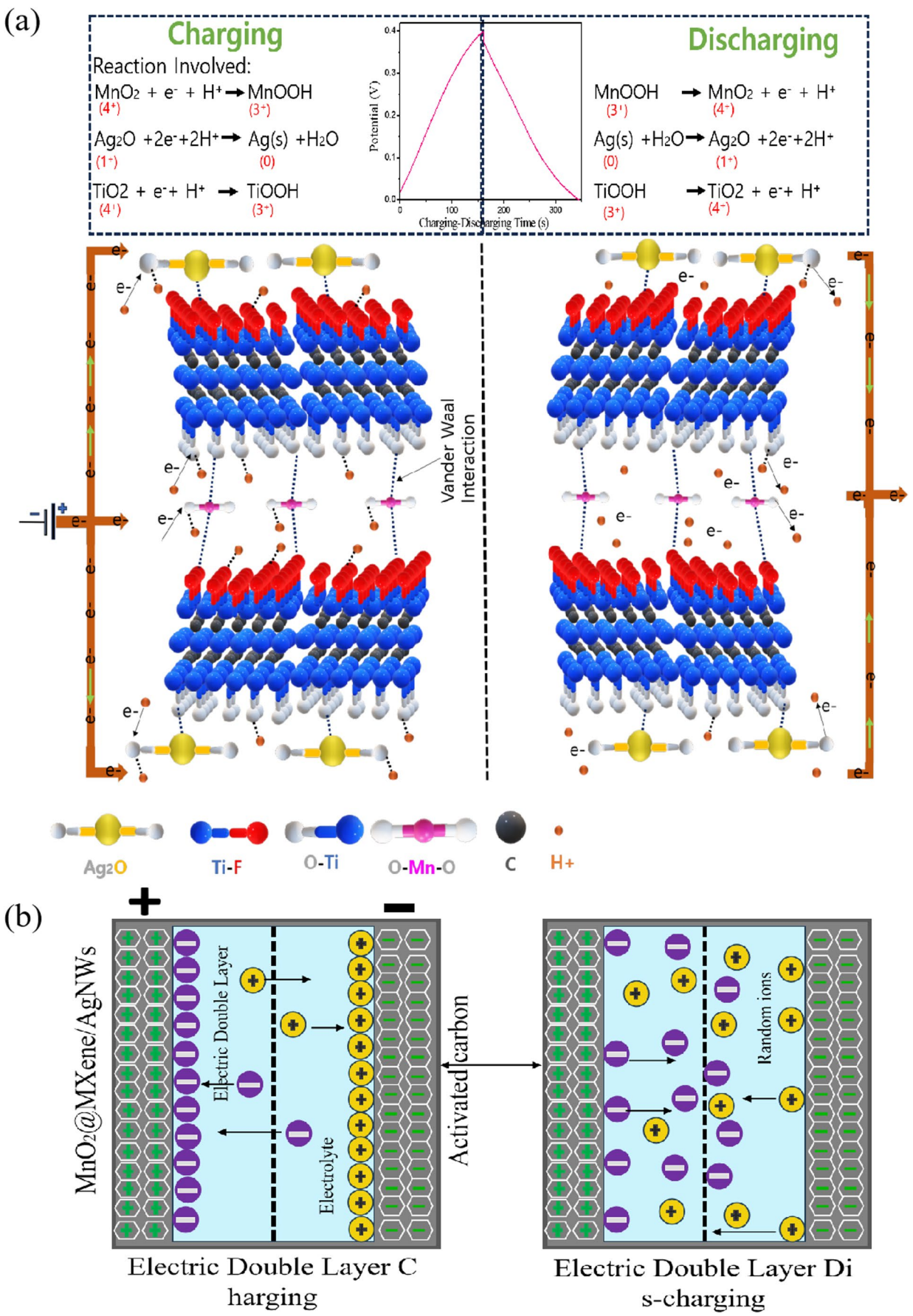

(a)
Charging
Reaction Involved:
MnO2 + e- + H+ → MnOOH
(4+) (3+)
Ag2O +2e-+2H+ → Ag(s) +H2O
(1+) (0)
TiO2 + e-+ H+ → TiOOH
(4+) (3+)
Potential (V)
Charging-Discharging Time (s)
Discharging
MnOOH → MnO2 + e- + H+
(3+) (4+)
Ag(s) +H2O → Ag2O +2e-+2H+
(0) (1+)
TiOOH → TiO2 + e-+ H+
(3+) (4+)
Vander Waal Interaction
e-
Ag2O
Ti-F
O-Ti
O-Mn-O
C
H+
(b)
+
−
MnO2@MXene/AgNWs
Electric Double Layer
Electrolyte
Activated carbon
Random ions
Electric Double Layer C harging
Electric Double Layer Di s-charging

Fig. 6 Redox-active charging–discharging mechanism of the MnO_2@MXene/AgNWs electrode in an acidic electrolyte (**a**), and EDLC-supported charge-storage mechanism based on MXene and AC (**b**)

ASC device can exhibit lower rate retention due to additional kinetic and resistance limitations, as well as possible mismatch between the positive and negative electrodes. Further optimization of electrode mass balance, interfacial contact, conductive pathways, and ion-transport channels would be beneficial for improving the rate performance of future ASC devices. The enhanced capacitive properties of the fabricated composite can be attributed to the synergistic effect of various 0D (MnO_2), 1D (AgNWs), and 2D (MXene) morphologies responsible for the enhanced surface area (13 m^2/g), reduced restacking and oxidation of the MXene sheets, and the combination of EDLC and redox active species.

To evaluate the percentage contribution of surface-controlled and diffusion-controlled mechanisms, Dunn's real method was employed. Figure 7g demonstrates a b value of 0.59, which lies between 0.5 and 1, indicating the presence of both diffusion and capacitive-controlled charge storage. However, the value is closer to 0.5, suggesting the predominance of diffusion-controlled charge storage, validating the presence of redox-active MnO_2. To assess the percentage contributions at various potentials, a bar graph was constructed in Fig. 7h. The composite exhibited 64.65%, 68.92%, 72.08%, 74.11%, 75.85%, 77.27%, 78.38%, 79.33%, and 80.44% capacitive-controlled charge storage mechanisms at 20, 30, 40, 50, 60, 70, 80, 90, and 100 mV s^{-1}, respectively. The results obtained followed the same trend as in the three-electrode system, where the capacitive-controlled contributions increased with increasing potential. This behavior can be attributed to the dominance of the surface at a higher potential and less time available for the ions to penetrate the MXene layers, which reduces the diffusion-controlled capacitance. However, the device possesses a higher percentage of capacitive control compared to the three-electrode system at all potentials, which can be attributed to the involvement of activated carbon as the negative electrode, which exhibits a characteristic EDLC charge storage mechanism. Subsequently, the reversibility of the ASC device was evaluated by calculating R^2 values for anodic and cathodic peak curves at various potentials (20–100 mV s^{-1}), as shown in Fig. 7i. The high R^2 values for both the anodic (0.995) and cathodic (0.993) currents indicate the excellent reversibility of the fabricated device.

Figure 7j and **k** illustrate the high C_a (565.1 mF cm^{-2} @ 6 mA cm^{-2}), E_a (~0.2 mWh cm^{-2}), and P_a (51.39 mW cm^{-2}) of the ASC device in comparison to previously reported MXene–based supercapacitors. Our ASC device exhibits the highest performance among all compared devices, which can be attributed to the synergistic 0D@2D/1D architecture. The further importance of the fabricated material can be seen via literature comparison in Table S2, where our material exhibits considerably high areal capacitance, areal energy density, cyclic and thermal stability.

Initially, four different ASC devices were fabricated using MXene, MXene/AgNWs, MnO_2@MXene, and MnO_2@MXene/AgNWs as positive electrodes and AC as the negative electrode. The CV curves of these devices were measured and compared, as shown in Figure S17. Among all devices, MnO_2@MXene/AgNWs//AC exhibited the largest CV area, consistent with the three-electrode results, further confirming the improved charge-storage capability of the final composite-based ASC device. Afterwards, all four devices were subjected to stability analysis for 10,000 GCD cycles at 5 mA $cm^{-2,}$ which can be depicted in Fig. 8. Figure 8a demonstrated that MXene, with a lack of chemical and mechanical stability, exhibits only 63.87% capacitance retention, which can be attributed to the absence of mechanical and chemical support to MXene via foreign particles. However, MXene/AgNWs showed little high capacitance retention (78.59%) compared to MXene alone, which may be due to the mechanical flexibility and high conductivity provided by the intercalated AgNWs, as presented in Fig. 8b. Moreover, MnO_2@MXene (Fig. 8c) and MnO_2@MXene/AgNWs (Fig. 8d) exhibit excellent capacitance retention of 99.0% and 98.52%, respectively, which can be attributed to the synergistic mechanical and chemical stability provided via decorated MnO_2 on the MXene sheets. The fact was supported by post-XPS analysis for all samples, where the Ti-H_2O and Ti-OH/O_x peak intensities and positions towards the x-axis (binding energies) were compared to analyze the extent of MXene oxidation (Ti oxidation state change) in the O 1 s spectrum of MXene, MXene/AgNWs, MnO_2@MXene, and MnO_2@MXene/AgNWs. Moreover, EIS analysis showed almost consistent R_{ct} value before (1.7 Ω) and after stability analysis (3.2 Ω) of MnO_2@MXene/AgNWs//AC device (Fig. 7l), which can be assigned to the desired stability achieved for MXene. Figure 8e presents the XPS spectrum of MXene with high intensities of Ti-H_2O and Ti-OH/O_x at the binding energies of 532.88 and 535.09 eV corresponds to the oxidation and oxygen rich terminations of MXene which can be due to higher oxidation states of oxidized Ti, likely, attributed to the stronger nucleus pull on remaining Ti valence electrons at higher oxidation state and responsible for higher binding energies for Ti-H_2O and Ti-OH/O_x [44]. However, the MXene/AgNWs spectrum in Fig. 8f showed less intensity for Ti-H_2O and Ti-OH/O_x at relatively lower binding energies of 532.6 and 534.78 eV, corresponding to the less oxidation of MXene in the composite compared to MXene alone, which can be due to the AgNWs oxidation avoiding the entire MXene oxidation, which is responsible for

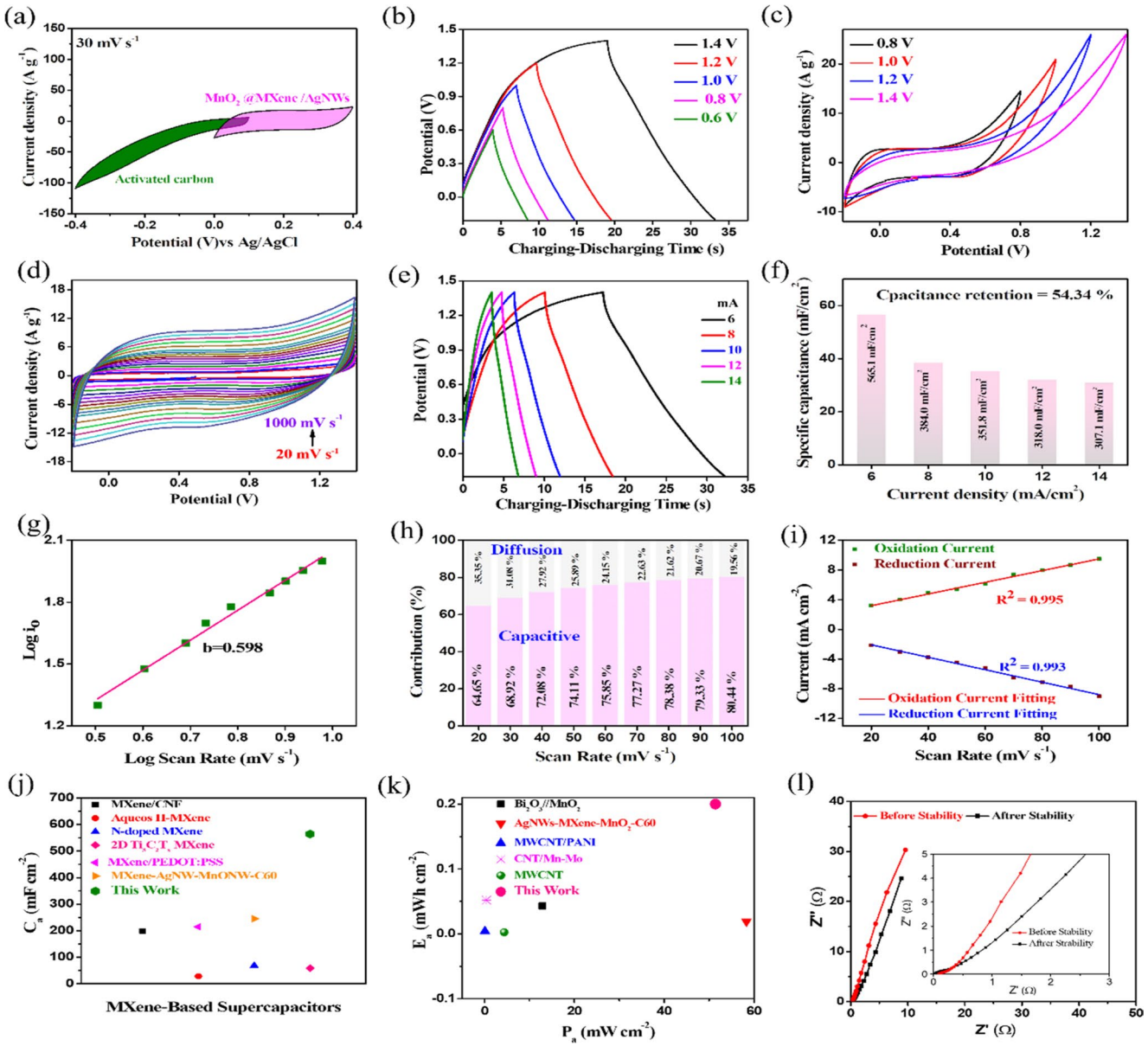


Fig. 7 Flexible ASC device with cathodic and anodic electrodes: (**a**) CV curves of the MnO_2@MXene/AgNWs (positive) and AC (negative) electrodes at a scan rate of 30 mV s^{-1}. (**b**) GCD curves of the ASC device at different potential windows from −0.2 to 0.6, 0.8, 1.0, 1.2, and 1.4 V. (**c**) CV curves of the ASC at the same potential windows. (**d**) CV curves of the ASC at scan rates from 20 to 1000 mV s^{-1}. (**e**) GCD curves of the ASC at current densities from 6 to 14 mA cm^{-2}. (**f**) Areal capacitance and capacitance retention of the ASC as a function of current density. (**g**) Relationship between log(i) and log(v) with the fitted b value. (**h**) Percentage contributions of capacitive- and diffusion-controlled charge storage at scan rates from 20 to 100 mV s^{-1} (**i**). Linear fitting of anodic and cathodic peak currents versus the square root of scan rate, illustrating the good reversibility of the fabricated ASC device. (**j**) Comparison of the areal capacitance (C_a) of this work with previously reported MXene-based supercapacitors, including MXene/CNF [39], N-doped MXene [40], MXene–AgNWs–MnO_2 NW–C60 [41], MXene/PEDOT: PSS [42], and 2D $Ti_3C_2T_x$ MXene [43]. (**k**) Ragone plot comparing the areal energy density (E_a) and areal power density (P_a) of this work with MXene/Fe_3O_4/MXene [44], MXene–rGO oxide [45], N-doped MXene [40], MXene–AgNWs–MnO_2 NW–C60 [41], and MXene/CNF/PC [46]. (**l**) Nyquist plots of the ASC device before and after the long-term cycling stability test

better capacitance retention as well [45]. Furthermore, the MnO_2@MXene sample (Fig. 8g) exhibits the lowest intensity for Ti-H_2O and Ti-OH/O_x at the lowest binding energies shift (531.63 and 532.77 eV), which demonstrates the MXene oxidation reduction in the presence of redox-active MnO_2. MXene in the presence of MnO_2 can reduce the oxidation (Ti^0 to $Ti^{2+, 3+, 4+}$) and oxygen-rich terminations of MXene, responsible for weak hold on valence electrons and demands lower energies for electron excitation for specific groups, which is higher in bare MXene and MXene/AgNWs. Due to this chemical support, the MnO_2@MXene composite exhibits 99.0% capacitance retention after

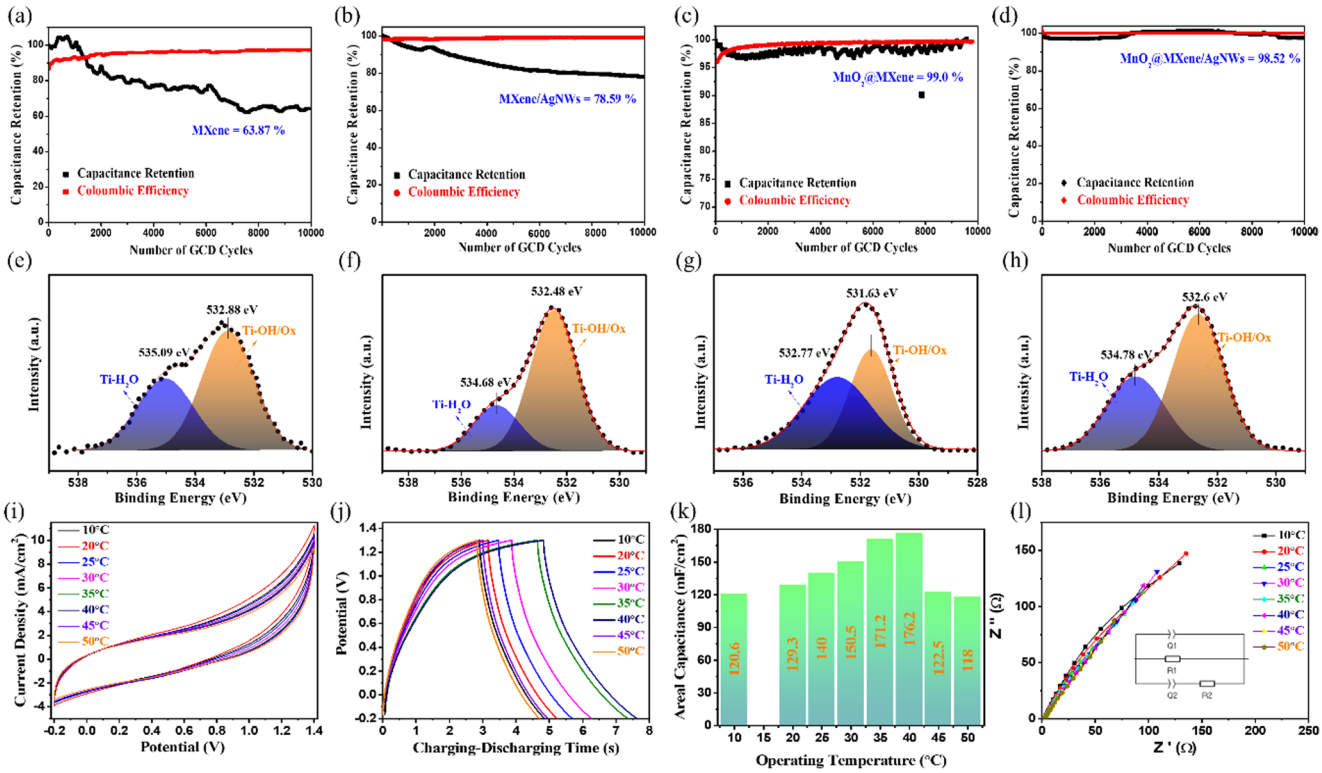


Fig. 8 Capacitance retention, and coulombic efficiency of MXene//AC (**a**), MXene/AgNWs//AC (**b**), MnO_2@MXene//AC (**c**), and MnO_2@MXene/AgNWs//AC (**d**) fabricated devices at the current density of 5 mA cm^{-2} for 10,000 GCD cycles, respectively. XPS spectrum of O 1 s for MXene (**e**), MXene/AgNWs (**f**), MnO_2@MXene (**g**), and MnO_2@MXene/AgNWs (**h**) after 10,000 GCD cycles at 5 mA cm^{-2} are presented to illustrate the oxygen environment around Ti after stability analysis in the presence of Ag and Mn, respectively. Cyclic voltammogram at 100 mV s^{-1} (**i**), GCD at 10 mA cm^{-2} (**j**), areal capacitance (**k**), and electrochemical impedance profiles (**l**) of 0D@2D/1D MXene-based asymmetric supercapacitors at different operating temperatures, such as 10, 20, 25, 30, 35, 40, 45, and 50 °C

10,000 GCD cycles, which demonstrates its utility to stabilize MXene from oxidation. Finally, the MnO_2@MXene/AgNWs exhibit 98.52% capacitance retention, higher than MXene (63.87%) and MXene/AgNWs (78.59%), which can be attributed to the incorporated MnO_2 oxidation. These oxidation mitigation and stable capacitance retention after MnO_2 incorporation into MXene/AgNWs composites further highlight the importance of MnO_2. The fact was further validated via the O 1 s spectrum, which retains low intensity for Ti-H_2O and Ti-OH/O_x at binding energies of 532.48 and 536.68 eV for the final composite (Fig. 8h), which is lower than MXene and MXene/AgNWs. Similarly, the all-fabricated devices exhibit 100% coulombic efficiency after 10,000 charging-discharging cycles, which indicates minimal electrode degradation and potential for long-term use. The stable performance, high capacitance retention, and coulombic efficiency of the final fabricated electrode (MnO_2@MXene/AgNWs) can be attributed to the morphological integrity of the composite provided via controlled morphological synthesis having specified dimensions. XPS spectrum of all samples after stability analysis was further deconvoluted into Ti 2p (Figure S18) for all four samples, Ag 3 d (Figure S19a) for MXene/AgNWs composite, Mn 2p (Figure S19b) for MnO_2@MXene, and MnO_2@MXene/AgNWs composites (Figure S20), the detailed description provided in Supporting information, Sect. 8.

Figure S18 shows the refitted Ti 2p spectra of MXene, MXene/AgNWs, MnO_2@MXene, and MnO_2@MXene/AgNWs after cyclic testing, with reference to previously reported MXene XPS fitting models [46, 47]. The relative peak-area ratios of Ti–C and TiO_2 components were compared to evaluate the oxidation degree of MXene. MXene exhibited severe oxidation after cycling, with a high TiO_2 ratio of 0.53 and a very low Ti–C ratio of 0.015. MXene/AgNWs showed a slightly lower TiO_2 ratio of 0.39 and a higher Ti–C ratio of 0.055, suggesting partial stabilization by the AgNW network. In contrast, MnO_2@MXene and MnO_2@MXene/AgNWs exhibited lower TiO_2 ratios of 0.32 and 0.33, respectively, together with higher Ti–C ratios of 0.17 and 0.12. The results indicate that MnO_2-containing composites can suppress irreversible MXene oxidation during cycling. Therefore, the improved capacitance retention and cycling stability of the MnO_2@MXene/AgNWs electrode can be attributed to the combined effects of suppressed MXene oxidation, improved electrical connectivity by AgNWs, and the structural stabilization of MXene sheets.

In addition, the Mn 2p spectra after cycling show the coexistence of Mn^{3+}/Mn^{4+} states in MnO_2@MXene and MnO_2@MXene/AgNWs composites (Figures S19 and S20), suggesting that MnO_2 remains redox-active during repeated charge–discharge processes. Together with the reduced TiO_2 ratios and higher Ti–C retention observed in the Ti 2p spectra, these results support the oxidation-mitigation role of MnO_2 rather than complete prevention of MXene oxidation.

The fact was further supported by FE-SEM, EDS, and XRD analysis after 10,000th GCD cycles of the final composite (MnO_2@MXene/AgNWs). The morphological stability of the fabricated material was checked through FE-SEM, as illustrated in Figure S21a. During the cyclic stability analysis, MXene usually undergoes restacking and morphological impairments, which mitigate its capacitance retention. The FE-SEM image clearly indicates that the incorporated MnO_2 NPs avoids restacking of MXene sheets, which provides 98.52% capacitance retention after 10,000 GCD cycles. Moreover, Figure S21b-j presents color mapping images to elucidate the elemental existence. The images aligned well with FE-SEM images with Ti and C as core elements, MnO_2 intercalated in between the layers, and AgNWs dispersed over the sheets. Figure S21k shows the EDS spectrum and elemental weight% of the final composite after 10,000 GCD cycles. The results demonstrate 18.61 Wt% of oxygen after the stability test, which is only 1.37 Wt% higher than the fresh composite, having an oxygen content of 17.24 Wt%, and corresponds well with post XPS analysis. Similarly, the XRD spectrum of MnO_2@MXene/AgNWs was conducted after 10,000 GCD cycles, as displayed in Figure S22. The XRD pattern shows all the characteristic peaks for MXene, MnO_2, and AgNWs correspond well with the XRD pattern conducted for the final sample (MnO_2@MXene/AgNWs) before stability test. These findings support the fact of structural stability provided by highly redox-active MnO_2. However, some anatase and rutile TiO_2 mixed phase peaks were observed at corresponding planes of (101), (202), and (110), (210) respectively. The observed peaks have very low intensities, suggesting minimal transformation of the Ti–C bond to Ti–O, which is consistent with EDS and XPS results. However, this transformation can have very little effect on the conductivity of the composite, which can be compensated by highly conductive AgNWs. Therefore, overall charge storage capability remained unaffected. To sum up, the variable and high oxidation state of MnO_2 makes it more readily available for oxidation-reduction in the MXene composite, resisting the oxidation of MXene ($Ti_3C_2 \rightarrow TiO_2$) and mitigating severe agglomeration via surface spacers, resultantly stabilizing MXene morphology, structure, and chemical nature (Ti_3C_2). Although AgNWs provide effective conductive pathways in the printed electrode, they are not fully chemically inert in strongly acidic H_2SO_4 electrolyte. Post-cycling morphology indicates partial fragmentation/degradation of AgNWs after prolonged operation, suggesting that AgNWs act mainly as conductive additives rather than long-term chemical stabilizers. Therefore, the improved cycling stability of MnO_2@MXene/AgNWs is primarily attributed to the MnO_2-stabilized MXene architecture, while AgNWs contribute mainly to enhanced electrical conductivity.

3.4 Application of the ASC device at varied temperature conditions

Operating temperature plays a significant role in the performance of supercapacitor material. MXene, with high temperature sensitivity due to its rapid conversion to TiO_2, exhibits poor stability at elevated temperatures. Herein, the stabilized MXene architecture through decorated MnO_2 nanoparticles performed well in a set of temperature ranges. The ASC device was fabricated and operated at 10, 20, 25, 30, 35, 40, 45, and 50 °C, respectively. Initially, the CV analysis of the device at all the above-mentioned temperatures was conducted at 100 mV s^{-1} and resulted in almost similar current densities and CV shapes (Fig. 8i). Thanks to the decorated MnO_2, which provides mechanical support to avoid morphological changes in MXene and oxidation scavenger for MXene. This gives a stable chemical nature to MXene at varied operating temperatures, making the fabricated MXene-based architecture feasible for different environmental conditions. Similarly, GCD analysis was conducted to verify the effect of operating temperature on charging and discharging time, where 25 °C (room temperature) was considered as the standard temperature and all measurements were conducted at 10 mA cm^{-1} (Fig. 8j). It can be depicted from Fig. 8j that at lower temperatures (10 °C and 20 °C) the charging and discharging time is relatively lower compared to room temperature, which can be due to the sluggish movement of electrolyte ions and less diffusion inside the MXene sheet. At elevated operating temperatures of 30, 35, and 40 °C, the GCD discharge time increased, indicating enhanced capacitive performance. Figure 8k shows the calculated areal capacitance at different operating temperatures, where the capacitance at 25 °C was used as the reference value (140 mF cm^{-2}, 100%). At lower temperatures of 10 and 20 °C, the areal capacitance decreased to 120.6 mF cm^{-2} (86.14%) and 129.3 mF cm^{-2} (92.35%), respectively, which can be attributed to sluggish electrolyte-ion kinetics and limited ion diffusion within the electrode. In contrast, the areal capacitance increased at 30, 35, and 40 °C to 150.5 mF cm^{-2} (107.5%), 171.2 mF cm^{-2} (122.28%), and 176.2 mF cm^{-2} (125.85%), respectively. This enhancement can be attributed to improved ion-transport kinetics and increased ionic conductivity of the PVA/H_2SO_4 gel electrolyte at

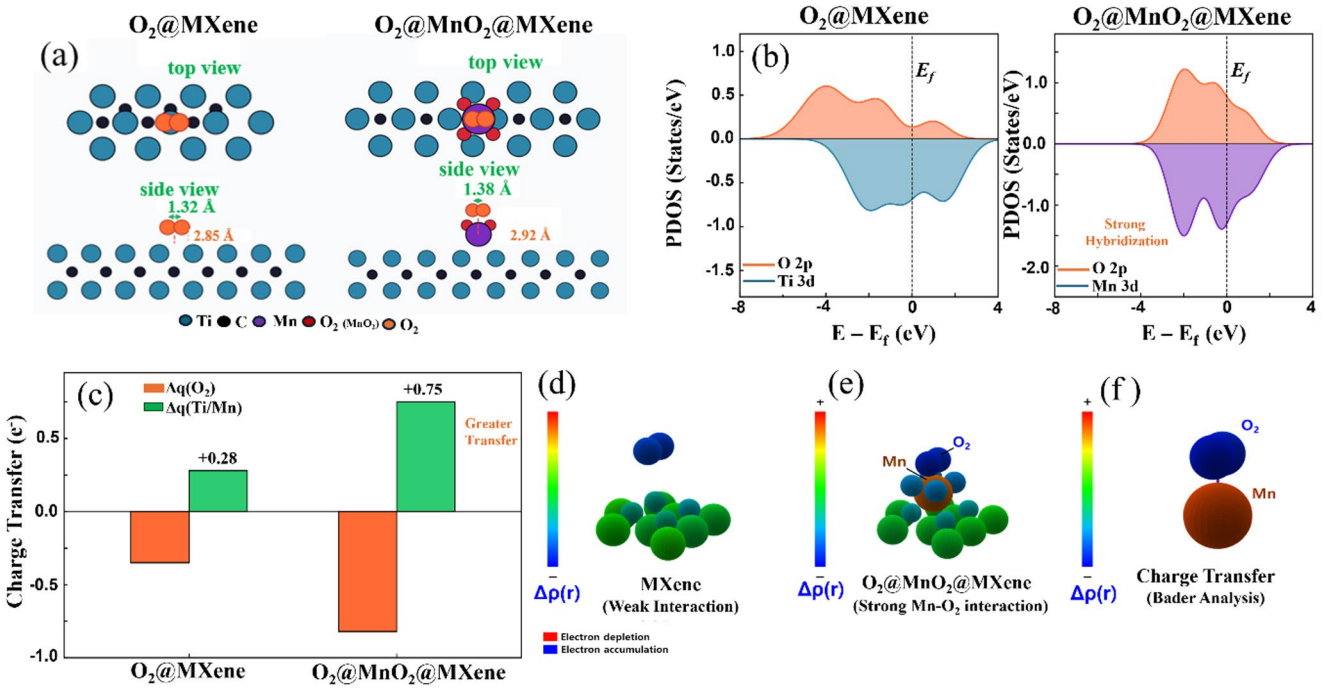


Fig. 9 Optimized geometries of O_2 adsorbed on MXene and MnO_2@MXene, showing that O_2 sits closer to Mn sites with a slightly elongated O-O bond (**a**). PDOS for O_2@$Ti_3C_2T_x$ and O_2@MnO_2@MXene. Stronger overlaps between O 2p and Mn 3 d states near EF indicate stronger MnO_2 bonding than for O 2p and Ti 3 d (**b**). Bader charge analysis giving the net charge gained by O_2 and lost by Ti or Mn. MnO_2@MXene exhibits much greater charge transfer, indicating that Mn acts as a sacrificial redox center (**c**). Charge density difference maps Delta rho(r) = rho(O_2@system) minus rho(system) minus rho(O_2) (**d**, **e**). Almost no redistribution is seen for $Ti_3C_2T_x$, while MnO_2@MXene shows electron accumulation around O2 and depletion at Mn. Schematic summary of the net charge transfer between Mn and O_2, consistent with the Bader results in panel (**f**, **c**)

moderately elevated temperatures. Higher temperature can increase the kinetic energy of electrolyte ions, reduce electrolyte viscosity, and enhance polymer chain segmental mobility, thereby promoting faster proton transport across the electrode/electrolyte interface and improving ion accessibility to electroactive sites [48]. This interpretation is supported by EIS fitting results, where the equivalent series resistance (R_s) values at 10, 20, and 25 °C were 2.17, 2.06, and 1.98 Ω, respectively, while the R_s values decreased to below 1.5 Ω at elevated temperatures (Fig. 8l**)**. However, when the temperature increased further to 45 and 50 °C, the areal capacitance decreased to 122.5 mF cm^{-2} (87.5%) and 118 mF cm^{-2} (84.24%), respectively. This decrease may be associated with thermally induced structural or chemical changes in the electrode/electrolyte system, which can offset the benefit of enhanced ion transport at higher temperatures. Overall, the fabricated MnO_2-stabilized MXene-based ASC device maintains considerable capacitance over a wide temperature range, indicating its potential for operation under varied environmental conditions. Figure 8l further shows the EIS profiles at different temperatures, with Rct values remaining in the range of approximately 2–4 Ω, suggesting relatively stable charge-transfer behavior across the tested temperature range.

3.5 DFT analysis of the oxygen scavenging mechanism

To gain microscopic insight into the improved oxidation stability of the MnO_2 modified MXene electrodes, density functional theory (DFT) calculations were carried out for O_2 adsorption on pristine MXene and on the MnO_2@MXene heterostructure. The optimized adsorption geometries are summarized in Fig. 9a. On the bare $Ti_3C_2T_x$ surface, the O_2 molecule resides relatively far from the surface Ti atoms and maintains a configuration that indicates weak interaction. In contrast, when MnO_2 is present, O_2 preferentially binds in the vicinity of the Mn centers, with a shorter O-Mn distance and a slightly elongated O-O bond, suggesting stronger chemisorption on the MnO_2 domain. The projected density of states in Fig. 9b reveals a clear difference in the electronic coupling between O_2 and the underlying metal sites. For O_2 adsorbed on $Ti_3C_2T_x$, the overlap between the O 2p states of the O_2 molecule and the Ti 3 d states of surface Ti atoms is relatively modest around the Fermi level. In contrast, the MnO_2@MXene system exhibits pronounced O 2p Mn 3 d hybridization near EF, indicating the formation of strongly bonded Mn O states. This enhanced hybridization implies that Mn-containing sites provide electronically favorable

adsorption sites for oxygen species, in agreement with the more negative O_2 adsorption energy on Mn sites compared to Ti sites, as shown in Figure S23a.

Bader charge analysis further quantifies the distinct charge transfer behavior, as summarized in Fig. 9c. For O_2@$Ti_3C_2T_x$, only a small amount of charge is transferred from Ti to the adsorbed O_2 molecule, consistent with weak oxidation of the Ti sites. In the O_2@MnO_2@MXene configuration, however, a substantially larger amount of charge is transferred from Mn atoms to O_2. This result demonstrates that Mn is preferentially oxidized and effectively acts as a sacrificial redox center, or oxygen scavenger, that buffers the oxidative attack on the conductive $Ti_3C_2T_x$ backbone. The real space charge density difference plots in Fig. 9d and e, and 9f provide a visual representation of this behavior. The pristine $Ti_3C_2T_x$ case shows negligible charge redistribution between O_2 and the surface, whereas the MnO_2@MXene case exhibits strong electron accumulation around O_2 accompanied by electron depletion at Mn sites, confirming the strong MnO_2 interaction inferred from the PDOS and Bader analyses. The total DOS comparison in Figure S23b further indicates that MnO_2 decoration introduces additional Mn 3d-derived states near the Fermi level, which likely facilitate this strong interaction with oxygen species. Overall, the DFT results consistently support the experimentally observed enhancement in oxidation resistance. MnO_2 domains serve not only as structural modifiers but also as chemically active oxygen scavengers that preferentially bind and consume oxygen species, thereby protecting the $Ti_3C_2T_x$ framework from degradation under ambient conditions.

4 Conclusion

A well-delaminated MXene was synthesized from the MAX phase as starting materials. The decoration of the MnO_2 NPs on the MXene sheets significantly mitigate the restacking of the MXene sheets and alleviate the oxidation of MXene during long-term cyclic stability and harsh environmental conditions, owing to the highly redox sponsor nature, which can shield the oxidation of MXene. Additionally, to enhance the rheological properties and conductivity of MnO_2@MXene, AgNWs were added to the as-synthesized MnO_2 decorated MXene to fabricate the MnO_2@MXene/AgNWs composite. Physicochemical characterizations confirm the synthesis of MXene, MXene/AgNWs, MnO_2@MXene, and MnO_2@MXene/AgNWs. The MnO_2@MXene/AgNWs exhibited the highest specific capacitance (878 F g^{-1} @ 0.5 A g^{-1}) and lowest impedance compared with MXene, MXene/AgNWs, and MnO_2@MXene, which ensures their potential practical applications. The combination of the AgNWs allows the direct printing of the MnO_2@MXene/AgNWs on a flexible PET substrate, and AC was printed as the cathodic material. The incorporation of highly conductive 1D-AgNWs makes the fabrication of the current collector-free supercapacitor possible. This simplifies the device architecture and is compatible with a scalable printing process. The ASC device demonstrated high C_a (565.1 mF cm^{-2} @ 6 mA cm^{-2}), E_a (~0.2 mWh cm^{-2}), P_a (51.39 mW cm^{-2}), cyclic stability (98.52%), and 86.14% (10 °C) and 84.24% (50 °C) capacitance retention at extreme environmental conditions. The role of MnO_2 to mitigate MXene oxidation was verified by examining the tested devices after 10,000 GCD cycles using XPS. The DFT simulation and post-cyclic characterization of the final composite using FE-SEM/EDS, XRD, and EIS further validate the role of MnO_2 in mitigating excessive MXene oxidation. These favorable characteristics of the material allow its practicality for printing and operations in harsh conditions; however, additional studies would be required to fully confirm the mechanisms.

Supplementary Information The online version contains supplementary material available at https://doi.org/10.1007/s42114-026-01862-z.

Acknowledgements This work was supported by the National Research Foundation of Korea (NRF) grant funded by the Government of Korea (NRF–RS–2024–00336593). This work was financially supported by the Global Research Development Center (GRDC) Cooperative Hub Program through the National Research Foundation of Korea (NRF) funded by the Ministry of Science and ICT (MSIT) (RS-2023-00257595).

Author contributions Ali Shan, Habibulla Imran, and Byungil Hwang: Conceptualization; Methodology; Formal analysis; Investigation; Resources; Visualization; Writings—original draft; Nida Nawaz, Chenhao Cong, and Seung Goo Lee: Investigation; Data curation; Writings—review & editing; Komal Golar, Mirza Mahmood Baig, and Hyungsub Yoon: Writings—review & editing; Jinhua Sun, Se Hyun Kim, and Sooman Lim: Conceptualization; Methodology; Resources; Funding acquisition; Writings—review & editing; Project administration; Supervision.

Funding Open access funding provided by Chalmers University of Technology. This work was supported by the National Research Foundation of Korea (NRF) grant funded by the Government of Korea (NRF–RS–2024–00336593). This work was financially supported by the Global Research Development Center (GRDC) Cooperative Hub Program through the National Research Foundation of Korea (NRF) funded by the Ministry of Science and ICT (MSIT) (RS-2023-00257595).

Data availability The data supporting the findings of this study are available from the corresponding author upon reasonable request.

Declarations

Competing interests The authors declare no competing interests.

Open Access This article is licensed under a Creative Commons Attribution 4.0 International License, which permits use, sharing, adaptation, distribution and reproduction in any medium or format, as long as you give appropriate credit to the original author(s) and the source, provide a link to the Creative Commons licence, and indicate if changes were made. The images or other third party material in this article are included in the article's Creative Commons licence, unless indicated otherwise in a credit line to the material. If material is not included in the article's Creative Commons licence and your intended use is not permitted by statutory regulation or exceeds the permitted use, you will need to obtain permission directly from the copyright holder. To view a copy of this licence, visit http://creativecommons.org/licenses/by/4.0/.

References

1. Wang M, Feng S, Bai C, Ji K, Zhang J, Wang S, Lu Y, Kong D (2023) Ultrastretchable MXene microsupercapacitors. Small 19:2300386
2. Li H, Liang J (2020) Recent development of printed micro-supercapacitors: printable materials, printing technologies, and perspectives. Adv Mater 32:1805864
3. Cao C, Tang S, Wu X, Huang H, Liu S, Li H (2025) Sustainable MXene/conductive cellulose heteroinks for 3D printed high areal energy density micro-supercapacitors and self-powered integrated systems. Adv Sci 12:e11439
4. Xue Y, Zhang Z, Liu D, Yang X, Wang C, Chen H, Zheng X, Li Q, Zhang T (2025) Advances in electrode and electrolyte materials of fiber-shaped supercapacitors for electrochemical performance improvement and applications extension. Energy Storage Mater 77:104222
5. Pacchioni G (2019) Superelectrodes for supercapacitors. Nat Rev Mater 4:625–625
6. Anasori B, Lukatskaya MR, Gogotsi Y 2D metal carbides and nitrides (MXenes) for energy storage, MXenes, Jenny Stanford Publishing2023, pp. 677–722
7. Choi, C., Qaiser, N. & Hwang, B. Mechanically pressed polymer-matrix composites with 3d structured filler networks for electromagnetic interference shielding application. Facta Universitatis, Series. Mech. Eng 22, 601–14 (2024).
8. Kim Y-J, Kim SJ, Seo D, Chae Y, Anayee M, Lee Y, Gogotsi Y, Ahn CW, Jung H-T (2021) Etching mechanism of monoatomic aluminum layers during MXene synthesis. Chem Mater 33:6346–6355
9. Pahlevaninezhad M, Sadri R, Momodu D, Eisawi K, Pahlevani M, Naguib M, Roberts EP (2024) Ammonium bifluoride-etched MXene modified electrode for the all− vanadium redox flow battery. Batteries Supercaps 7:e202300473
10. Liu L, Zschiesche H, Antonietti M, Gibilaro M, Chamelot P, Massot L, Rozier P, Taberna P, Simon P (2023) In situ synthesis of MXene with tunable morphology by electrochemical etching of MAX phase prepared in molten salt. Adv Energy Mater 13:2203805
11. Gurzęda B, Boulanger N, Nordenström A, Dejoie C, Talyzin AV (2024) Pristine MXene: in situ XRD study of MAX phase etching with HCl+LiF solution. Adv Sci 11:2408448
12. Zhu X, Yang K, Zhang Z, He S, Shen Z, Jiang W, Huang Y, Xu Y, Jiang Q, Pan L (2024) Additive-free anode with high stability: Nb2CTx MXene prepared by HCl-LiF hydrothermal etching for lithium-ion batteries. ACS Appl Mater Interfaces. https://doi.org/10.1021/acsami.4c05140
13. Zhu X, Yang K, Zhang Z, He S, Shen Z, Jiang W, Huang Y, Xu Y, Jiang Q, Pan L (2024) Additive-free anode with high stability: Nb_2CT_x MXene prepared by HCl-LiF hydrothermal etching for Lithium-ion batteries. ACS Appl Mater Interfaces 16:28709–28718
14. Mahmood M, Rasheed A, Ayman I, Rasheed T, Munir S, Ajmal S, Agboola PO, Warsi MF, Shahid M (2021) Synthesis of ultrathin MnO_2 nanowire-intercalated 2D-MXenes for high-performance hybrid supercapacitors. Energy Fuels 35:3469–3478
15. Li Y, Pan C, Kamdem P, Jin X-J (2020) Binder-free two-dimensional MXene/acid activated carbon for high-performance supercapacitors and methylene blue adsorption. Energy Fuels 34:10120–10130
16. Li S, Shi Q, Li Y, Yang J, Chang TH, Jiang J, Chen PY (2020) Intercalation of metal ions into $Ti_3C_2T_x$ MXene electrodes for high-areal-capacitance microsupercapacitors with neutral multivalent electrolytes. Adv Funct Mater 30:2003721
17. Prenger K, Sun Y, Ganeshan K, Al-Temimy A, Liang K, Dun C, Urban JJ, Xiao J, Petit T, Van Duin AC (2022) Metal cation pre-intercalated $Ti_3C_2T_x$ MXene as ultra-high areal capacitance electrodes for aqueous supercapacitors. ACS Appl Energy Mater 5:9373–9382
18. Luo Y, Tang Y, Bin X, Xia C, Que W (2022) 3D porous compact 1D/2D Fe_2O_3/MXene composite aerogel film electrodes for all-solid-state supercapacitors. Small 18:2204917
19. Zhang Y, Cao J, Yuan Z, Zhao L, Wang L, Han W (2021) Assembling Co_3O_4 nanoparticles into MXene with enhanced electrochemical performance for advanced asymmetric supercapacitors. J Colloid Interface Sci 599:109–118
20. Chavan RA, Kamble GP, Dhavale SB, Rasal AS, Kolekar SS, Chang J-Y, Ghule AV (2023) NiO@ MXene nanocomposite as an anode with enhanced energy density for asymmetric supercapacitors. Energy Fuels 37:4658–4670
21. Shan A, Imran H, Batool K, Lim S (2025) Fabrication of flexible and bendable solid state symmetric supercapacitor based on carbon black intercalated MXene. J Energy Storage 125:117019
22. Kumar N, Gajraj V, Upadhyay S, Chetana S, Sankaranarayanan S, Hossain I, Joshi NC, Priyadarshi N, Sen A (2023) One-step fragmentation of a 2D MXene across the fine 1D MnO_2 surface and its supercapacitance. CrystEngComm 25:72–85
23. Chen L, Tiwari SR, Zhang Y, Zhang J, Sun Y (2021) Facile synthesis of hollow MnO_2 nanoparticles for reactive oxygen species scavenging in osteoarthritis. ACS Biomater Sci Eng 7:1686–1692
24. Yu L, Hu L, Anasori B, Liu Y-T, Zhu Q, Zhang P, Gogotsi Y, Xu B (2018) MXene-bonded activated carbon as a flexible electrode for high-performance supercapacitors. ACS Energy Lett 3:1597–1603
25. Yang K, Luo M, Zhang D, Liu C, Li Z, Wang L, Chen W, Zhou X (2022) $Ti_3C_2T_x$/carbon nanotube/porous carbon film for flexible supercapacitor. Chem Eng J 427:132002
26. Luo Y, Que W, Nugraha AS, Kang Y, Tang Y, Wu Z, Henzie J, Yamauchi Y (2025) Mesoporous gold decorated MXene ($Ti_3C_2T_x$) flexible composite films for photo-enhanced solid-state micro-supercapacitors. J Mater Chem A 13:1330–1342
27. Li H, Li X, Liang J, Chen Y (2019) Hydrous RuO_2-decorated MXene coordinating with silver nanowire inks enabling fully printed micro-supercapacitors with extraordinary volumetric performance. Adv Energy Mater 9:1803987
28. Cao Z, Zhu YB, Chen K, Wang Q, Li Y, Xing X, Ru J, Meng LG, Shu J, Shpigel N (2024) Super-stretchable and high-energy micro-pseudocapacitors based on MXene embedded Ag nanoparticles. Adv Mater 36:2401271
29. Zhang CJ, McKeon L, Kremer MP, Park S-H, Ronan O, Seral-Ascaso A, Barwich S, Coileáin CÓ, McEvoy N, Nerl HC (2023) Additive-free MXene inks and direct printing of micro-supercapacitors, MXenes. Jenny Stanford Publishing, pp 463–485
30. Lim KRG, Shekhirev M, Wyatt BC, Anasori B, Gogotsi Y, Seh ZW (2022) Fundamentals of MXene synthesis. Nat Synth 1:601–614

31. Zhang X, Zhang W, Zhao H (2022) Electrochemical performance of $Ti_3C_2T_x$ MXenes obtained via ultrasound assisted LiF-HCl method. Mater Today Commun 33:104384
32. Parker T, Zhang D, Bugallo D, Shevchuk K, Downes M, Valurouthu G, Inman A, Chacon B, Zhang T, Shuck CE (2024) Fourier-transform infrared spectral library of MXenes. Chem Mater 36:8437–8446
33. Rita A, Sivakumar A, Dhas SSJ, Dhas SMB (2020) Structural, optical and magnetic properties of silver oxide (AgO) nanoparticles at shocked conditions. J Nanostruct Chem 10:309–316
34. Cao Y, Deng Q, Liu Z, Shen D, Wang T, Huang Q, Du S, Jiang N, Lin C-T, Yu J (2017) Enhanced thermal properties of poly (vinylidene fluoride) composites with ultrathin nanosheets of MXene. RSC Adv 7:20494–20501
35. Kalkal A, Tiwari A, Sharma D, Baghel MK, Kumar P, Pradhan R, Packirisamy G (2023) Air-brush spray coated Ti_3C_2-MXene-graphene nanohybrid thin film based electrochemical biosensor for cancer biomarker detection. Int J Biol Macromol 253:127260
36. Liu Y, Zhang G, Zuo C, Zhao K, Zeng J, Yin J, Chen H, Xie S, Qiu Y (2020) Core-shell AgNWs@Ni $(OH)_2$ nanowires anchored on filter paper for efficient hydrogen evolution reaction. J Electrochem Soc 167:116520
37. Zhou H, Han SJ, Lee HD, Zhang D, Anayee M, Jo SH, Gogotsi Y, Lee TW (2022) Overcoming the limitations of MXene electrodes for solution-processed optoelectronic devices. Adv. Mater. 34:2206377
38. Baig MM, Zulfiqar S, Yousuf MA, Shakir I, Aboud MFA, Warsi MF (2021) $Dy_xMnFe_{2-x}O_4$ nanoparticles decorated over mesoporous silica for environmental remediation applications. J. Hazard. Mater. 402:123526
39. Ghidiu M, Lukatskaya MR, Zhao M-Q, Gogotsi Y, Barsoum MW Conductive two-dimensional titanium carbide 'clay'with high volumetric capacitance, MXenes, Jenny Stanford Publishing2023, pp. 379–399
40. Zhang C, Anasori B, Seral-Ascaso A, Park SH, McEvoy N, Shmeliov A, Duesberg GS, Coleman JN, Gogotsi Y, Nicolosi V (2017) Transparent, flexible, and conductive 2D titanium carbide (MXene) films with high volumetric capacitance. Adv. Mater. 29:1702678
41. Zeng Z, Sun P, Zhu J, Zhu X (2015) Ag-doped manganese oxide prepared by electrochemical deposition on carbon fiber for supercapacitors. RSC Adv 5:17550–17558
42. Patil R, Pradhan L, Matsagar BM, Agrawal O, Wu K-W, Jena BK, Dutta S (2023) High-performance asymmetric supercapacitor device with Nickel–Cobalt bimetallic sites encapsulated in multilayered nanotubes. Energy Adv 2:1650–1659
43. Zhang QZ, Zhang D, Miao ZC, Zhang XL, Chou SL (2018) Research progress in MnO_2–carbon based supercapacitor electrode materials. Small 14:1702883
44. Brette F, Célérier S, Canaff C, Loupias L, Paris M, Habrioux A, Boucher F, Mauchamp V (2025) XPS binding energy shifts in 2D $Ti_3C_2T_z$ MXene go largely beyond intuitive explanations: rationalization from DFT simulations and experiments. Small Methods 9:2400848
45. Guan P, Zhu R, Zhu Y, Chen F, Wan T, Xu Z, Joshi R, Han Z, Hu L, Wu T (2022) Performance degradation and mitigation strategies of silver nanowire networks: a review. Crit Rev Solid State Mater Sci 47:435–459
46. Wen D, Wang X, Liu L, Hu C, Sun C, Wu Y, Zhao Y, Zhang J, Liu X, Ying G (2021) Inkjet printing transparent and conductive MXene ($Ti_3C_2T_x$) films: a strategy for flexible energy storage devices. ACS Appl Mater Interfaces 13:17766–17780
47. Natu V, Benchakar M, Canaff C, Habrioux A, Célérier S, Barsoum MW (2021) A critical analysis of the X-ray photoelectron spectra of $Ti_3C_2T_z$ MXenes. Matter 4:1224–1251
48. Zhang LL, Zhao X (2009) Carbon-based materials as supercapacitor electrodes. Chem Soc Rev 38:2520–2531

Publisher's note Springer Nature remains neutral with regard to jurisdictional claims in published maps and institutional affiliations.